

Electron Heating in Magnetosheath Turbulence: Dominant Role of the Parallel Electric Field within Coherent Structures

Qianyun Xu¹, Meng Zhou¹, Wenqing Ma², Jiansen He³, Shiyong Huang⁴, Zhihong Zhong¹, Ye Pang¹, and Xiaohua Deng¹

¹Nanchang University

²Nanchang university

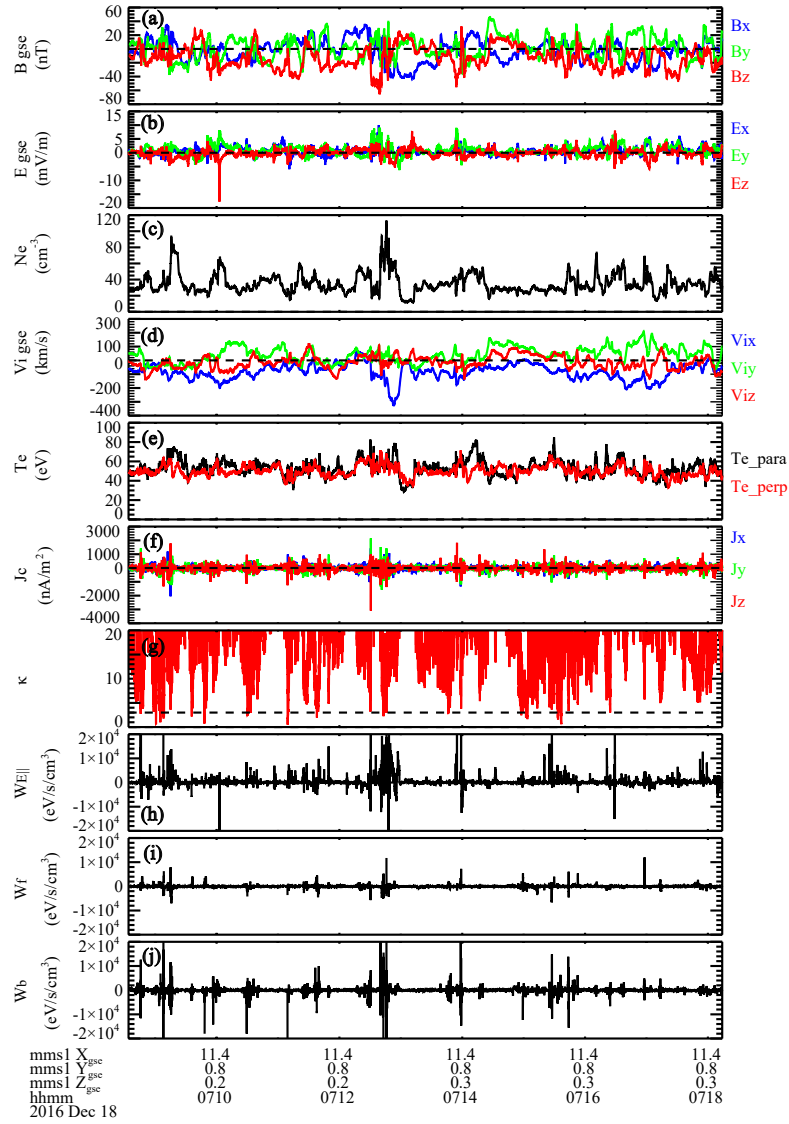
³Peking University

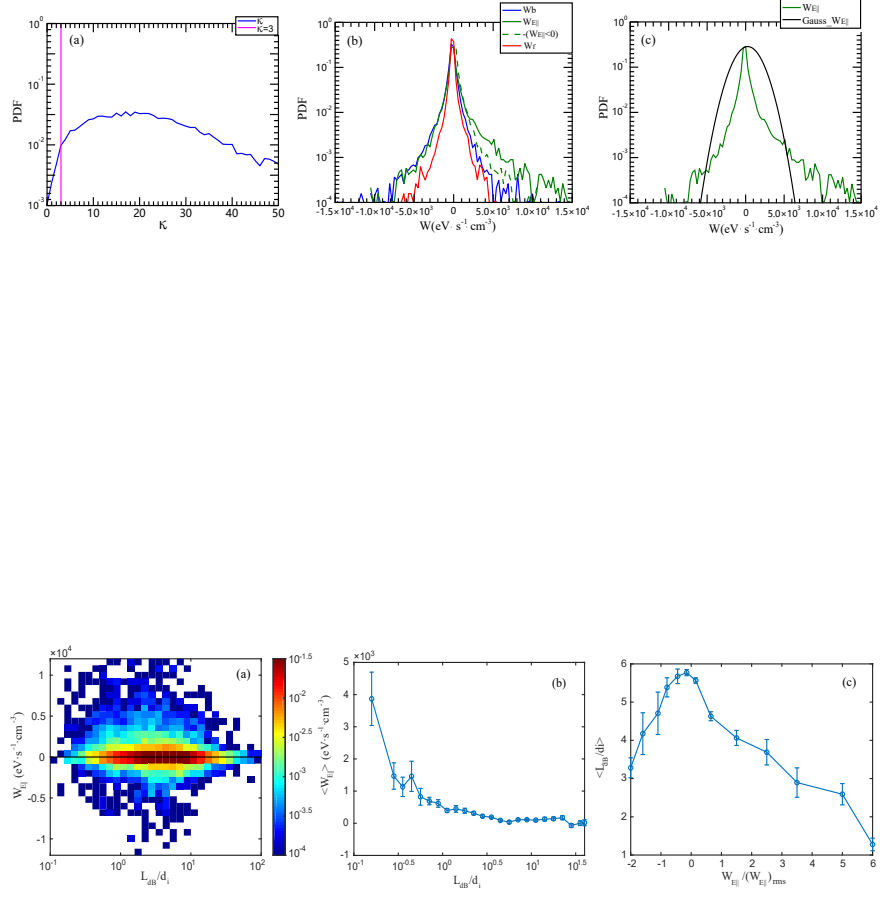
⁴Wuhan University

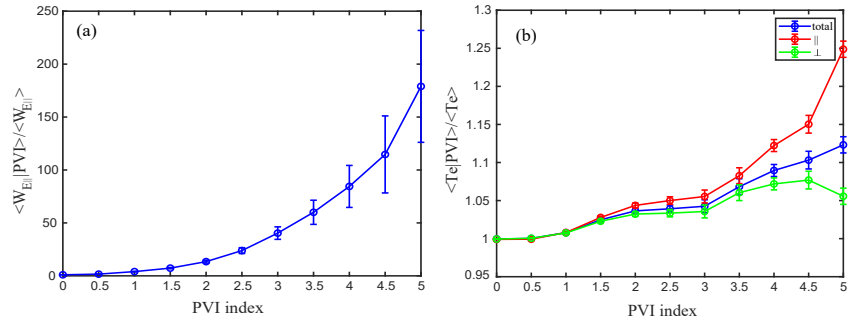
December 16, 2022

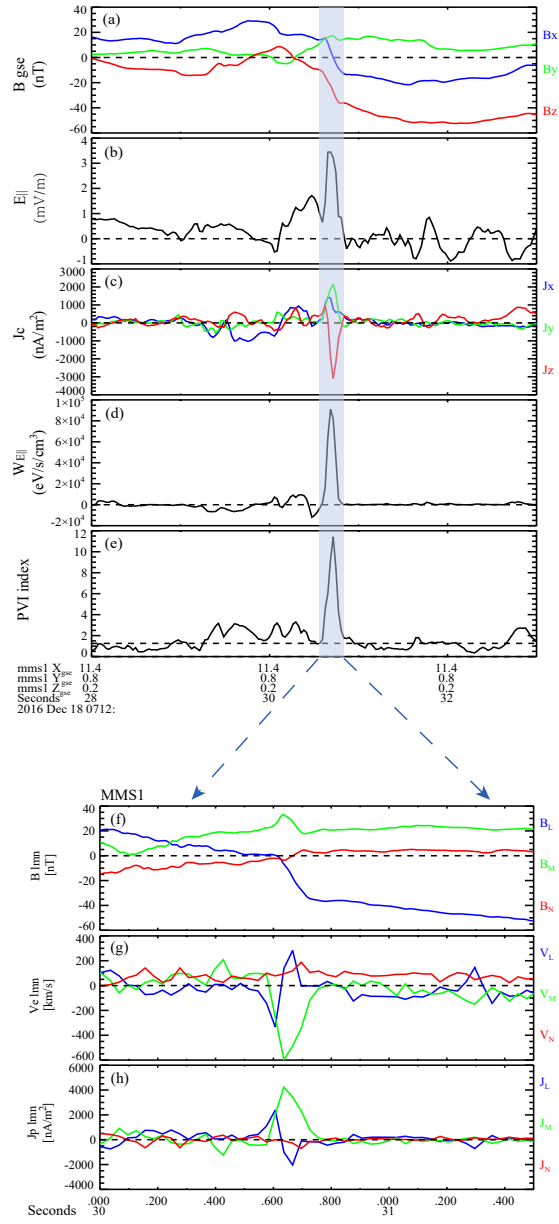
Abstract

How are particles being energized by turbulent electromagnetic fields is an outstanding question in plasma physics and astrophysics. This paper investigates the electron acceleration mechanism in strong turbulence ($\delta B/B_0 \sim 1$) in the Earth's magnetosheath based on the novel observations of the Magnetospheric Multiscale (MMS) mission. We find that electrons are magnetized in turbulent fields for the majority of the time. By directly calculating the electron acceleration rate from Fermi, betatron mechanism, and parallel electric field, it is found that electrons are primarily accelerated by the parallel electric field within coherent structures. Moreover, the acceleration rate by parallel electric fields increases as the spatial scale reduces, with the most intense acceleration occurring over about one ion inertial length. This study is an important step towards fully understanding the turbulent energy dissipation in weakly collisional plasmas.









1 **Electron Heating in Magnetosheath Turbulence: Dominant Role of** 2 **the Parallel Electric Field within Coherent Structures**

3 Qianyun Xu^{1,2}, Meng Zhou^{1,2}, Wenqing Ma², Jiansen He³,
4 Shiyong Huang⁴, Zhihong Zhong^{1,2}, Ye Pang², Xiaohua Deng²

5
6 1. Department of Physics, School of Physics and Materials Science, Nanchang
7 University, Nanchang 330031, People's Republic of China;

8 2. Institute of Space Science and Technology, Nanchang University, Nanchang
9 330031, People's Republic of China;

10 3. School of Earth and Space Sciences, Peking University, Beijing 100871, People's
11 Republic of China;

12 4. School of Electronic Information, Wuhan University, Wuhan, People's Republic
13 of China;

14 **Key points:**

- 15 1. Electrons are primarily accelerated by the parallel electric field in the
16 magnetosheath turbulence.
- 17 2. The E_{\parallel} acceleration mostly occurs within the coherent structures through Joule-type
18 dissipation.
- 19 3. The average E_{\parallel} acceleration rate increases with the decreasing local spatial scale.

20 **Abstract**

21 How are particles being energized by turbulent electromagnetic fields is an
22 outstanding question in plasma physics and astrophysics. This paper investigates the
23 electron acceleration mechanism in strong turbulence ($\delta B/B_0 \sim 1$) in the Earth's
24 magnetosheath based on the novel observations of the Magnetospheric Multiscale
25 (MMS) mission. We find that electrons are magnetized in turbulent fields for the
26 majority of the time. By directly calculating the electron acceleration rate from Fermi,
27 betatron mechanism, and parallel electric field, it is found that electrons are primarily
28 accelerated by the parallel electric field within coherent structures. Moreover, the
29 acceleration rate by parallel electric fields increases as the spatial scale reduces, with

30 the most intense acceleration occurring over about one ion inertial length. This study is
31 an important step towards fully understanding the turbulent energy dissipation in
32 weakly collisional plasmas.

33 **Plain language summary**

34 The magnetosheath is one of the most turbulent environments in near-Earth space,
35 which is very beneficial to the study of collisionless turbulent plasma. The mechanism
36 of turbulent energy dissipation and the consequent plasma heating is not fully
37 understood. The Magnetosphere Multiscale mission provides high-time cadence data
38 and simultaneous multi-spacecraft measurements at very small inter-spacecraft
39 separations. That can measure important quantities related to dissipation and heating at
40 kinetic scales. This paper investigates how electrons are being accelerated through the
41 dissipation of magnetic energy in nonlinear turbulence in the Earth's magnetosheath.
42 We classify the acceleration mechanisms into three types: Fermi mechanism, betatron
43 mechanism, and E_{\parallel} acceleration. By directly calculating and comparing these
44 mechanisms, we find electrons are predominantly accelerated by parallel electric fields
45 within coherent structures. The E_{\parallel} acceleration is the most effective around the ion
46 inertial length.

47

48 **1. Introduction**

49 Energy cascade is one of the most prominent features of turbulence. Energy is
50 injected at large scales, like fluid scales, then cascades to small scales through non-
51 linear interactions, and finally dissipated at kinetic scales, leading to plasma heating
52 and particle acceleration and the formation of suprathermal tails in the particle energy
53 spectrum (Kiyani et al., 2015). Space plasma is typical of weak collisionality; hence
54 collisionless mechanisms play a critical role in turbulent energy dissipation in space
55 plasmas (Matthaeus et al., 2015; Chen 2016; Howes 2017). How the particles are
56 heated/accelerated by turbulence is one of the most outstanding questions in plasma
57 turbulence; however, the mechanism of turbulent energy dissipation and the consequent
58 plasma heating is not fully understood after decades of intensive study.

59 Different types of acceleration mechanisms have been proposed to explain plasma

60 heating by the turbulent cascade in collisionless plasma. These mechanisms can be
61 generally classified into two categories: resonant acceleration and non-resonant
62 acceleration. The dissipation of waves is usually due to the energy transfer to energizing
63 particles caused by field and particle resonance, which can work over a long distance
64 and a long time. It includes Landau damping, cyclotron damping, and transit-time
65 damping (Chandran et al., 2010; Dmitruk et al., 2004a; Sahraoui et al., 2009; Isenberg
66 & Hollweg 1983; Gary et al., 2000; Isenberg 2001; Marsch & Tu 2001; Klein et al.,
67 2017). Previous studies have found clues of this resonant acceleration in space plasma
68 turbulence. He et al. (2015a, 2015b) suggested that solar wind ions are heated by
69 Landau damping and cyclotron damping by identifying characteristic signatures of
70 these resonances in the ion velocity distribution functions. Recently, in situ signature of
71 cyclotron resonant heating in the solar wind turbulence is observed by Parker Solar
72 Probe observations (Bowen et al., 2022). Chen et al. (2019) presented direct evidence
73 for Landau damping in magnetosheath turbulence by using the novel field-particle
74 correlation technique. The Landau damping mechanism for electron heating is further
75 confirmed by examining more events in the magnetosheath using the same field-particle
76 correlation method (Afshari et al., 2021).

77 One typical non-resonant acceleration is stochastic heating, which heats plasma
78 when the motion of particles becomes chaotic as the amplitude of electromagnetic field
79 fluctuations, at scales comparable to the gyro-scale, exceeds a critical value (Chandran
80 et al., 2010; Vech et al., 2017). It is found that acceleration and dissipation also occur
81 in coherent structures, such as current sheets (Retinò et al., 2007; Dmitruk et al., 2004b;
82 Osman et al., 2012), magnetic islands (Huang et al., 2016), small-scale vortices
83 (Alexandrova & Saur 2008), and magnetic holes (Huang et al., 2017a, 2017b; Zhong et
84 al., 2019), etc. It is suggested that magnetic reconnection occurring within the current
85 sheets in turbulence provides an important pathway for energy dissipation (Osman et
86 al., 2014; Zhou et al., 2021). The correlation between energy dissipation and localized
87 coherent structures indicates that energy dissipation may occur non-uniformly.

88 The motivation of this study is to investigate the acceleration and heating of electrons
89 in plasma turbulence. Different from Chen et al. (2019) and Afshari et al. (2021), the

90 turbulent interval we examine in this paper has large fluctuations with $\delta B/B_0 \sim 1$. In
 91 addition, we not only quantify the electron acceleration rate by the parallel electric field,
 92 as has been done by Chen et al. (2019) and Afshari et al. (2021), but also quantify the
 93 acceleration by the perpendicular electric field. The electron acceleration rates are
 94 evaluated under the guiding center approximation. We have used the data from the
 95 Magnetospheric Multiscale (MMS) mission, which provides high-time cadence data
 96 and simultaneous multi-spacecraft measurements at very small inter-spacecraft
 97 separations. This combination enables the study of the nature of dissipation at kinetic
 98 scales with an unprecedented level of accuracy and resolution. The FGM magnetic field
 99 instruments (Russell et al., 2016), EDP electric field instruments (Ergun et al., 2016;
 100 Lindqvist et al., 2016), and FPI ion and electron detectors (Pollock et al., 2016) provide
 101 the high-resolution data required to characterize signatures of dissipation and heating.

102

103 **2. Methodology**

104 Here we employ the method that has been used to calculate the acceleration rate in
 105 reconnection. This method considers the particle energy gain under guiding center
 106 approximation (Dahlin et al., 2014; Zhou et al., 2018; Zhong et al., 2020; Ma et al.,
 107 2020, 2022). The integrated energy gain of electrons in a unit volume per unit time for
 108 betatron acceleration is given by:

$$109 \quad W_b = P_{e\perp} \mathbf{v}_{E \times B} \cdot \frac{\nabla \mathbf{B}}{B} + \frac{P_{e\perp}}{B} \frac{\partial B}{\partial t} \quad (1)$$

110 where $P_{e\perp}$ is the perpendicular electron pressure, $\mathbf{v}_{E \times B}$ is the $E \times B$ drift speed, $\nabla \mathbf{B}$ is
 111 the gradient of the total magnetic field. We refer to W_b as the betatron acceleration
 112 rate hereafter. Betatron acceleration might be efficient in magnetosheath turbulence,
 113 which usually involves large-amplitude $|B|$ fluctuations, such as magnetic holes and
 114 magnetic peaks (e.g., Huang et al., 2017a, 2017b; Yao et al., 2018).

115 The Fermi acceleration rate is calculated by

$$116 \quad W_f = (P_{e\parallel} + n_e m_e v_{e\parallel}^2) \mathbf{v}_{E \times B} \cdot (\mathbf{b} \cdot \nabla \mathbf{b}) \quad (2)$$

117 where $P_{e\parallel}$ is the electron parallel pressure, $v_{e\parallel}$ is the electron parallel bulk velocity and
 118 \mathbf{b} is the unit vector of the magnetic field. Fermi acceleration is essentially caused by the

119 curvature drift in motional curved field lines. In situ observations in the magnetosheath
 120 suggest that curvature drift acceleration may be important for particle energization in
 121 magnetized turbulence (Bandyopadhyay et al., 2020; Huang et al., 2020).

122 The E_{\parallel} acceleration rate, which is caused by the parallel electric field, is given by

$$123 \quad W_{E_{\parallel}} = J_{e\parallel} E_{\parallel} + \frac{\beta_{e\perp}}{2} J_{\parallel} E_{\parallel} \quad (3)$$

124 where $\beta_{e\perp}$ is the ratio between the perpendicular electron pressure and the magnetic
 125 pressure, J_{\parallel} is the total parallel current density and $J_{e\parallel}$ is the parallel current carried by
 126 electrons. The presence of $\frac{\beta_{e\perp}}{2} J_{\parallel} E_{\parallel}$ is to eliminate the work caused by the parallel
 127 magnetization drift.

128 Betatron and Fermi mechanisms cause the heating of plasmas while E_{\parallel} leads to not
 129 only plasma heating but also plasma bulk acceleration. The heating of plasma by E_{\parallel} can
 130 be understood by examining the electron momentum equation:

$$131 \quad E_{\parallel} = -\frac{1}{en} (\nabla \cdot \mathbf{P}_e)_{\parallel} - \frac{m_e}{e} \left(\frac{dv_e}{dt} \right)_{\parallel} \quad (4)$$

132 where e is the unit charge, n is the number density, v_e is the electron bulk velocity and
 133 \mathbf{P}_e is the electron pressure tensor. The relationship between the parallel electric field
 134 and the electron energy gain can be obtained by multiplying Eq. (4) by $-nev_{e\parallel}$:

$$135 \quad -nev_e E_{\parallel} = v_{e\parallel} (\nabla \cdot \mathbf{P}_e)_{\parallel} + nm_e v_{e\parallel} \left(\frac{dv_e}{dt} \right)_{\parallel} \quad (5)$$

136 The first term on the RHS of Eq. (5) contributes to the thermal energy increase of
 137 electrons, i.e., electron heating, while the second term on the RHS of Eq. (5) is related
 138 to the electron bulk velocity variation.

139 Equations (1) – (3) can be used to evaluate the acceleration rates for the three
 140 different types of mechanisms when the electrons satisfy the guiding center
 141 approximation, i.e., they are magnetized, or say, the 1st adiabatic invariant is conserved.
 142 To test this criterion, we calculate κ (Büchner & Zelenyi 1989):

$$143 \quad \kappa_{\text{curv}} = \sqrt{R_c / \rho_e} \quad (6)$$

144 where R_c is the curvature radius of the magnetic field, and ρ_e is the electron gyration
 145 radius, which is calculated by using four times the electron temperature, higher than the
 146 energy of most electrons in the magnetosheath. When $\kappa > 3$, electrons of the specific

147 energy are considered to satisfy the guiding center approximation. In the following
148 study, we calculate the acceleration rates only at times when κ is greater than 3.

149

150 **3. Results**

151 Figure 1 shows the overview of the MMS observations in a turbulent magnetosheath
152 from 07:08:14 to 07:18:34 UT on 2016 December 18. The location of the MMS
153 spacecraft in the geocentric solar ecliptic (GSE) coordinate system is [11.4, 0.8, 0.2] R_E
154 (R_E is earth radii), downstream of the quasi-perpendicular bow shock. The average
155 spacing of the MMS tetrahedron is $\sim 8.5 \text{ km} \sim 9.5 d_e$ given the average plasma density
156 of $\sim 35 \text{ cm}^{-3}$, where d_e is the electron inertial length. The tetrahedron quality factor (TQF)
157 is ~ 0.99 , indicating that the four satellites constitute a nearly perfect tetrahedron in
158 space. One can see from Figures 1a-1c that the electromagnetic fields and plasma flows
159 are highly turbulent. The electron flow speed is similar to that of the ion flow, except
160 that electron bulk velocity has some high-frequency fluctuations, which leads to
161 filamentary currents with peak density larger than 500 nA m^{-2} (Figure 1f). The electron
162 temperature exhibits an anisotropy with $T_{e\parallel} > T_{e\perp}$ in this interval (Figure 1g). The average
163 ion bulk velocity is about 120 km s^{-1} and the average electron temperature is about 50
164 eV.

165 Figure 1g shows that κ is larger than 3 (the black dotted line) for most of the time.
166 This can be also clearly seen in the probability distribution function (PDF) of the κ
167 values displayed in Figure 2a. About 99% of κ are greater than 3, which means that
168 electrons are magnetized almost during the entire interval. The PDF of κ increases from
169 nearly 0 and reaches the peak at around $\kappa=18$, then it monotonically descends as the
170 increment of κ . Figures 1h-1j display the electron acceleration rates for the three
171 different acceleration mechanisms. They have both positive and negative values,
172 suggesting bi-directional energy exchange between the electromagnetic fields and
173 electrons rather than unidirectional energy conversion. The largest acceleration rate is
174 up to $2 \times 10^4 \text{ eV s}^{-1} \text{ cm}^{-3} \sim 3.2 \text{ nW m}^{-3}$. There are many spikes in accelerated rates, which
175 is the manifestation of intermittency. Note that the above three acceleration rates are

176 calculated in the frame co-moving with the magnetosheath flow, that is, $\mathbf{E}' = \mathbf{E} + \langle \mathbf{V} \rangle \times$
177 \mathbf{B} , where $\langle \mathbf{V} \rangle$ is the average ion bulk velocity in the whole interval.

178 To determine the main acceleration mechanism, we plot the PDF of the three
179 acceleration rates in Figure 2b. The total number of data points is about 20,000. We see
180 that the highest value of the PDF is around $W=0$. The PDFs are sign-indefinite, which
181 implies that the energy exchange between electromagnetic fields and plasmas goes both
182 ways. The PDF of $W_{E_{\parallel}}$ is the broadest among the three, indicating that E_{\parallel} acceleration
183 is generally greater than the other two mechanisms. The PDF of $W_{E_{\parallel}}$ is asymmetric with
184 respect to $W=0$, with a higher positive tail, while the PDF of W_b shows a subtle heavier
185 negative tail and the PDF of W_f is nearly symmetric to $W=0$. The average acceleration
186 rate of E_{\parallel} , betatron, and Fermi acceleration is $278 \text{ eV s}^{-1} \text{ cm}^{-3}$, $-77 \text{ eV s}^{-1} \text{ cm}^{-3}$, and -4
187 $\text{eV s}^{-1} \text{ cm}^{-3}$, respectively. Therefore, on average, electrons were accelerated by E_{\parallel} ,
188 whereas betatron and Fermi mechanisms decelerated the electrons. The average
189 energization rate of electrons by E_{\parallel} is at least one order of magnitude larger than the
190 results reported in previous literature (Afshari et al., 2021; Bandyopadhyay et al., 2020).
191 The PDF of $W_{E_{\parallel}}$ is non-Gaussian with a heavier tail (Figure 2c), suggesting the
192 intermittent nature of the acceleration process (Matthaeus et al., 2015). The
193 intermittency is further proved by the large kurtosis of the E_{\parallel} , betatron, and Fermi
194 acceleration rate, which is 374, 196, and 72, respectively.

195 Since the acceleration of electrons is dominated by parallel electric fields, we mainly
196 focus on E_{\parallel} acceleration in the following. To understand at which scale the acceleration
197 occurs, we estimate the spatial scale of the magnetic field $L_{dB} = B/|\nabla \mathbf{B}|$ using the
198 multi-spacecraft measurements under the assumption that the spatial variation is linear
199 inside the MMS tetrahedron (Chanteur 1998). Here, $|\nabla \mathbf{B}|$ is the norm of the Jacobian
200 matrix of the magnetic field, i.e., $|\nabla \mathbf{B}| = \sqrt{\sum_{ij} (\frac{\partial B_i}{\partial x_j})^2}$ (Kress et al. 2007). Figure 3a
201 shows the joint PDF of the E_{\parallel} acceleration rate $W_{E_{\parallel}}$ and the L_{dB} . We see that most of the
202 data points are near $W_{E_{\parallel}}=0$, which is consistent with Figure 2b. L_{dB} is typically larger
203 than $\sim 0.3 d_i$ and smaller than $30 d_i$. Figure 3b points out that the average acceleration
204 rate descends with the increment of the spatial scale, from larger than $1000 \text{ eV s}^{-1} \text{ cm}^{-3}$

205 when $L_{dB} < 10^{-0.5} d_i$ to less than $200 \text{ eV s}^{-1} \text{ cm}^{-3}$ when $L_{dB} > 10 d_i$. Figure 3c displays
 206 that the average L_{dB} is the largest near $W_{E||}=0$ and descends toward larger $W_{E||}$ in both
 207 the positive and negative directions. The average L_{dB} reduces to about $1 d_i$ when $W_{E||}$ is
 208 6 times larger than its RMS.

209 The Partial Variance of Increments (PVI) method has been widely used to identify
 210 the coherent structures in turbulent plasma (Matthaeus et al., 2015; Greco et al., 2009,
 211 2018; Chasapis et al., 2015). The PVI index can be calculated using magnetic fields
 212 observed by multi-spacecraft:

$$213 \quad PVI_{ij}(t) = \sqrt{\frac{|B^i(t) - B^j(t)|^2}{\langle |B^i(t) - B^j(t)|^2 \rangle}} \quad (7)$$

214 where the subscript $i, j=1,2,3,4$ indicates the different spacecraft. Figure 4a shows the
 215 $E_{||}$ acceleration rate conditioned on the PVI index. We see that the average $W_{E||}$
 216 monotonically increases with the increment of PVI index, which means that the most
 217 intense $E_{||}$ acceleration corresponds to the largest PVI index. The average $W_{E||}$ with PVI
 218 index >3 is about 40 times the $W_{E||}$ averaged over all the data points. We also examine
 219 the local increase of the electron temperature conditioned on the PVI index (Figure 4b).
 220 The local increase of the electron temperature is represented by the electron temperature
 221 normalized by its regional average. It shows that similar to the profile of $W_{E||}$, the
 222 average T_e also increases nearly monotonically with the increase of the PVI index.
 223 Notice that the monotonic trend is clearer in $T_{e||}$ than in $T_{e\perp}$. This is consistent with
 224 previous observations that strong electron heating, measured by the local increase of
 225 the electron temperature, occurs within current sheets with large PVI index, while no
 226 apparent heating within current sheets with small PVI index (Chasapis et al., 2015;
 227 Huang et al., 2022). Here we go one step further by confirming that structures with
 228 larger PVI index contribute to greater energy dissipation and electron acceleration.

229 Moreover, we investigate where the most intense $E_{||}$ acceleration occurs. We define
 230 the intense $E_{||}$ acceleration event as the interval in which the peak $W_{E||}$ is greater than
 231 $5,100 \text{ eV s}^{-1} \text{ cm}^{-3}$. This value is the intersection of the PDF of $W_{E||}$ and the Gaussian
 232 curve in Figure 2c. The boundary of each event is set as $5100/e \approx 1,900$, where e is the

233 natural exponential. We identify the coherent structures when the PVI index is larger
234 than the threshold $\langle PVI \rangle + \sigma(PVI) \sim 1.3$, where $\langle PVI \rangle$ and $\sigma(PVI)$ are the average and
235 standard deviation of PVI index in the entire interval (Greco et al., 2009). Finally, 68
236 intense E_{\parallel} acceleration events were selected, with 60 events having a PVI index greater
237 than the threshold, i.e., they are within the coherent structures. One can see from Figure
238 3a that data points with $W_{E_{\parallel}}$ larger than $5,100 \text{ eV s}^{-1} \text{ cm}^{-3}$ are mostly in the range $L_{\text{dB}} \sim$
239 $[1, 10] \text{ d}_i$.

240 Figure 5 shows one example of intense E_{\parallel} acceleration events. It is shown that the
241 intense E_{\parallel} acceleration was coincident with a large PVI index, which corresponds to a
242 coherent structure with a sharp change of the magnetic field and an intense current. A
243 unipolar $E_{\parallel} \sim 3 \text{ mV m}^{-1}$ was responsible for $\sim 8 \times 10^4 \text{ eV s}^{-1} \text{ cm}^{-3}$ acceleration rate in the
244 parallel direction. Moreover, we transfer the magnetic field, electron bulk flow, and
245 electric current to the local LMN coordinates (Figure 5g-5i) to see whether this event
246 was associated with a local reconnection. We employ the same procedure as Man et al.
247 (2022) to identify local reconnection, such as the electron outflowing jets and the out-
248 of-plane current supporting the magnetic field reversal. We see a clear electron bulk
249 flow reversal corresponding well to the current sheet crossing, implying that MMS
250 encountered an active reconnection in this coherent structure. We have further
251 examined all the intense E_{\parallel} acceleration events. Overall, 30 ($\sim 44\%$) intense E_{\parallel}
252 acceleration events are associated with local reconnection. Therefore, we conclude that
253 reconnection plays a significant role in accelerating electrons in this event.

254

255 **4. Discussion and Conclusion**

256 We have analyzed 31 other intervals in the turbulent magnetosheath observed by
257 MMS from the year 2015 to 2019 (Wang et al., 2021). Twenty-two of these intervals
258 are downstream of the quasi-parallel bow shock, and the other 9 events are downstream
259 of the quasi-perpendicular bow shock. These events have a broader range of plasma β .
260 We analyze these events by the same method described in this paper and find
261 qualitatively similar results, that is, electrons are predominantly accelerated by E_{\parallel} no

262 matter whether the interval is downstream of the quasi-parallel or quasi-perpendicular
263 bow shock.

264 A further question that needs to be addressed is whether the E_{\parallel} acceleration in the
265 coherent structures is due to Landau damping, stochastic heating, or Joule-type
266 dissipation. Since the electrons are magnetized most of the time, they could not be
267 energized through stochastic heating, which requires that the electron magnetic moment
268 is not conserved (e.g., Vech et al., 2017). This event is different from the events reported
269 by Afshari et al. (2021) and Chen et al. (2019), which demonstrate that electrons were
270 accelerated through Landau resonance with the kinetic Alfvén waves. One major
271 difference is that the magnetic field is relatively stable and has few coherent structures
272 in the events studied by Afshari et al. (2021). This is also manifested by the non-
273 Gaussian PDF of the E_{\parallel} acceleration rate in our event, whereas the PDF is near Gaussian
274 in turbulence dominated by Landau damping (not shown). Importantly, we find that the
275 large E_{\parallel} acceleration studied in this paper is usually associated with unipolar E_{\parallel} rather
276 than wave-like E_{\parallel} . Thus, the E_{\parallel} acceleration observed in our event is unlikely caused by
277 Landau damping. More detailed analysis using the field-particle correlation technique
278 for each intense E_{\parallel} acceleration event can be performed to further understand E_{\parallel}
279 acceleration in these coherent structures.

280 In summary, we have investigated how electrons are being accelerated through the
281 dissipation of magnetic energy in nonlinear turbulence in the Earth's magnetosheath.
282 Since electrons are mostly magnetized, we classify the acceleration mechanisms into
283 three types: Fermi process, betatron mechanism, and E_{\parallel} acceleration. We find that the
284 PDF of E_{\parallel} acceleration is significantly broader than the PDF of the other two
285 acceleration rates, which implies that electrons are predominantly accelerated by
286 parallel electric fields. $W_{E_{\parallel}}$ increases with the reduction of the spatial scale and the
287 increment of the PVI index, suggesting that the E_{\parallel} acceleration is the most effective
288 around the ion inertial length and coherent structures play a vital role in energizing
289 electrons through E_{\parallel} . We demonstrate that electrons are accelerated through Joule-type
290 dissipation/heating in strong turbulence containing many coherent structures, which is
291 another important building block of the particle energization physical scenario besides

292 the mechanism proposed by Chen et al. (2019) and Afshari et al. (2021).

293 The acceleration and heating of ions by turbulence may be quite different to the
294 electrons because ions are expected to be demagnetized due to their much larger gyro-
295 radius. Hence one cannot use the guiding center approximation to describe the ion
296 motion and may resort to other methods to quantify the ion acceleration, which is
297 underway for further report.

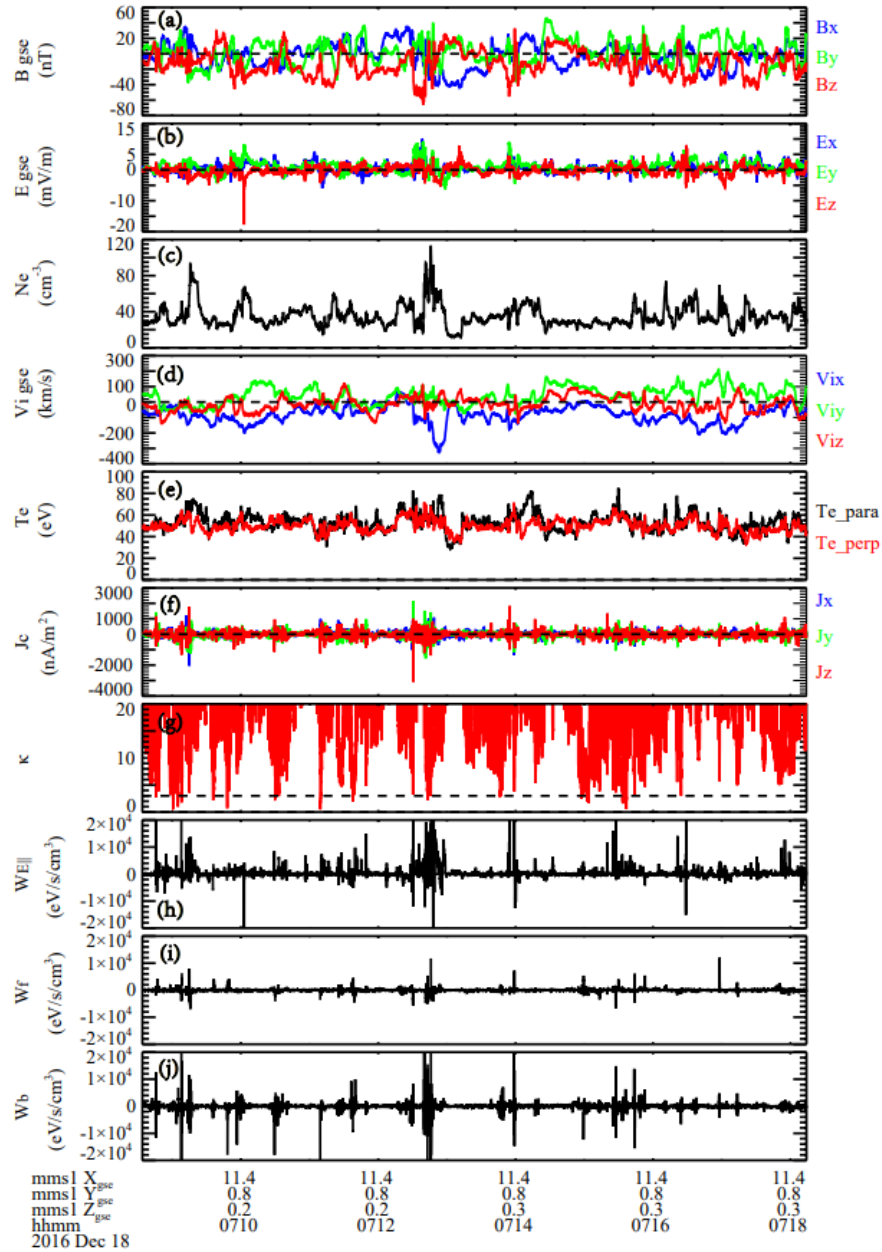
298

299 **Acknowledgments**

300 Thanks to the MMS team for providing the high-quality data to complete this work.
301 This work is supported by the National Natural Science Foundation of China (NSFC)
302 under grant Nos. 42074197, 42130211, and 41774154.

303 **Data Availability Statement**

304 The data used in this study was obtained from the MMS Science Data Center
305 (<https://lasp.colorado.edu/mms/sdc/public/about/browse-wrapper/>).

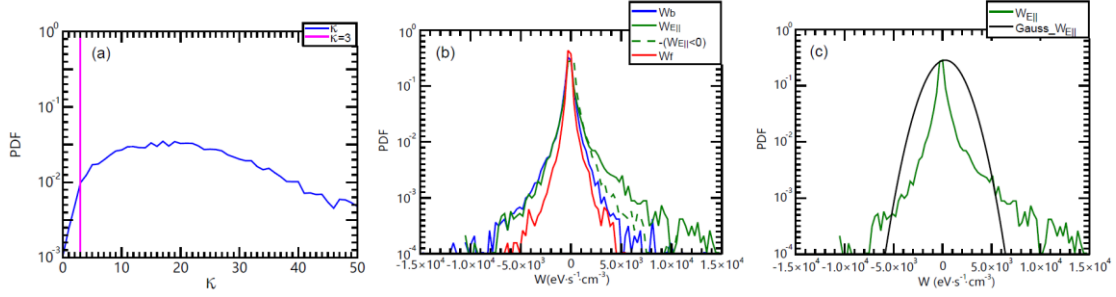


306

307 **Figure 1.** Overview of the turbulence in the magnetosheath observed by MMS from
 308 07:08:14 to 07:18:34 UT on 18 December 2016. From the top to bottom are: (a) three
 309 components of the magnetic field and (b) the electric field; (c) electron number density;
 310 (d) ion bulk velocity; (e) electron parallel and perpendicular temperatures; (f) electric
 311 current density; (g) κ value; (h) – (j) the acceleration rate from E_{\parallel} , Fermi process and
 312 betatron mechanism, respectively. The vectors are displayed in the GSE coordinate
 313 system.

314

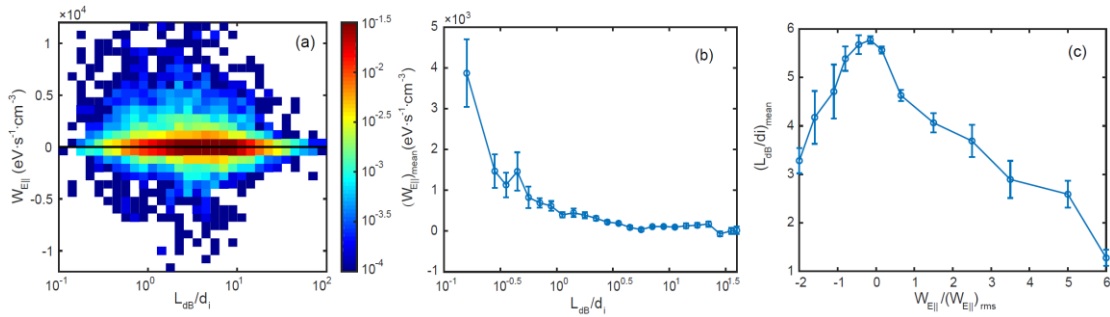
315



316

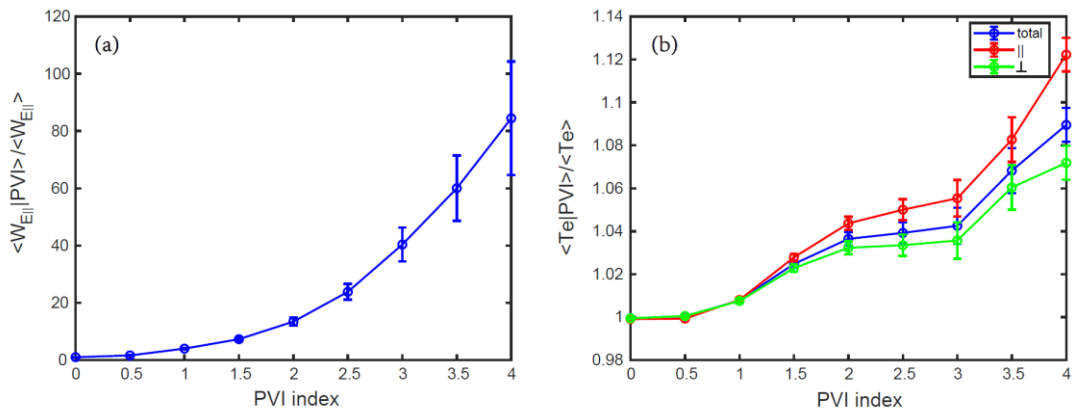
317 **Figure 2.** (a) probability distribution function (PDF) of κ . The pink line marks $\kappa=3$; (b)
 318 PDF of betatron acceleration rate (blue), Fermi acceleration rate (red) and the E_{\parallel}
 319 acceleration rate (green). The green dashed line is the mirror image of the negative E_{\parallel}
 320 acceleration rate; (c) comparison of the PDF of the E_{\parallel} acceleration rate and the Gaussian
 321 curve (black).

322



323

324 **Figure 3.** (a) Joint PDFs of E_{\parallel} acceleration rate and the local magnetic field scale L_{dB} ;
 325 (b) the average $W_{E_{\parallel}}$ as a function of L_{dB} ; (c) the average L_{dB} as a function of
 326 $W_{E_{\parallel}}/(W_{E_{\parallel}})_{rms}$, here $(W_{E_{\parallel}})_{rms}$ is the root mean square of $W_{E_{\parallel}}$; The vertical bars in panels
 327 (b) and (c) represent the standard errors of the mean.

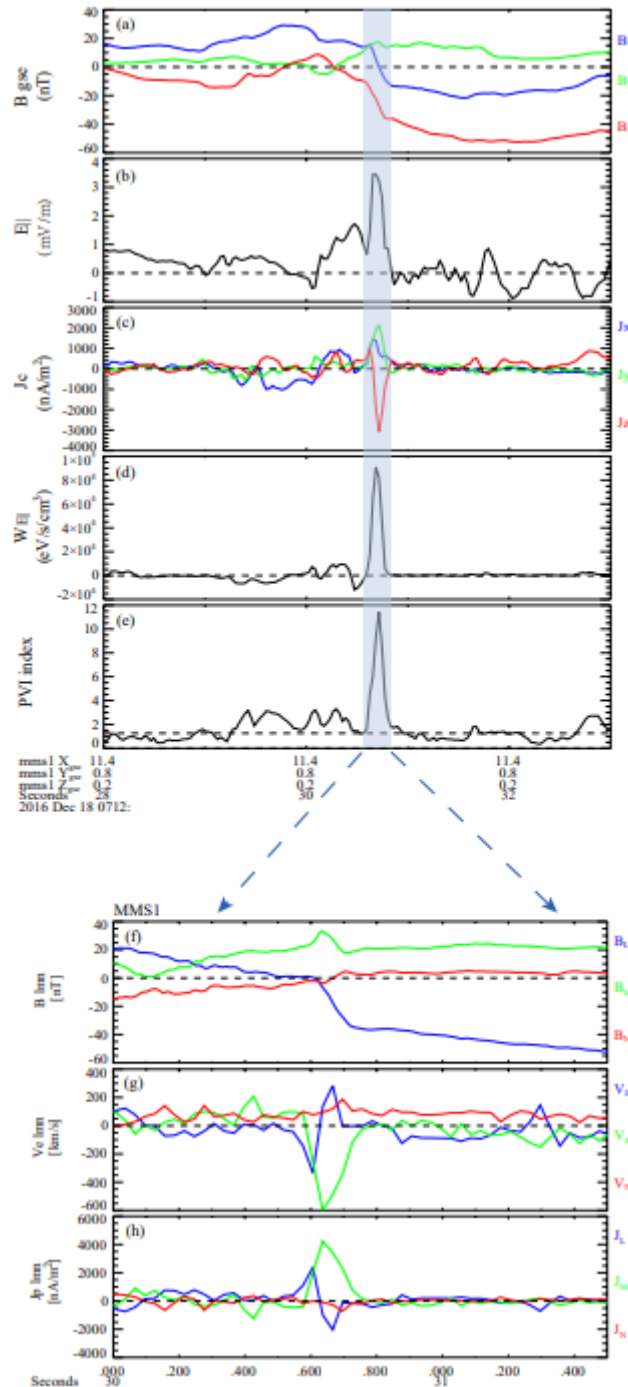


328

329 **Figure 4.** Average E_{\parallel} acceleration rate (a) and electron temperature (b) conditioned on
 330 the binned PVI index. The average $W_{E_{\parallel}}$ is normalized by the averaged value in the entire

331 interval. The electron temperature is normalized by $\langle T_e \rangle$ in a moving window with
 332 duration of 4 s, equivalent to approximately 10 d_i . The vertical bars represent the
 333 standard error of the mean.

334



335

336 **Figure 5.** An example of the intense $E_{||}$ accelerate event. From the top to bottom are:
 337 (a) three components of the magnetic field; (b) parallel electric field; (c) electric current
 338 density; (d) $E_{||}$ acceleration rate; (e) PVI Index. The shaded area highlights a significant

339 electron accelerate by E_{\parallel} within a coherent structure. The expanded view displays the
340 (f) magnetic field; (g) electron bulk velocity and (h) current density in the LMN
341 coordinate system around the coherent structure.

342

343 **References**

344 [1] Afshari, A. S., Howes, G. G., Kletzing, C. A., Hartley, D. P., & Boardsen, S. A.
345 (2021). The importance of electron Landau damping for the dissipation of turbulent
346 energy in terrestrial magnetosheath plasma. *Journal of Geophysical Research: Space*
347 *Physics*, 126(12), e2021JA029578. <https://doi.org/10.1029/2021JA029577>

348 [2] Alexandrova, O., & Saur, J. (2008). Alfvén vortices in Saturn's magnetosheath:
349 Cassini observations. *Geophysical Research Letters*, 35(15).
350 <https://doi.org/10.1029/2008GL034411>

351 [3] Bandyopadhyay, R., Matthaeus, W. H., Parashar, T. N., Yang, Y., Chasapis, A., Giles,
352 B. L., Gershman, D. J., Pollock, C. J., Russell, C. T., Strangeway, R. J., Torbert, R. B.,
353 Moore, T. E., & Burch, J. L. (2020). Statistics of kinetic dissipation in Earth's
354 magnetosheath: MMS observations. *Physical Review Letters*, 124(25), 255101.
355 <https://doi.org/10.1103/PhysRevLett.124.255101>

356 [4] Bowen, T. A., Chandran, B. D., Squire, J., Bale, S. D., Duan, D., Klein, K. G., Larson,
357 D., Mallet, A., McManus, M. D., Meyrand, R., et al. (2022). In Situ Signature of
358 Cyclotron Resonant Heating in the Solar Wind. *Physical Review Letters*, 129(16),
359 165101.

360 [5] Büchner, J., & Zelenyi, L. M. (1989). Regular and chaotic charged particle motion
361 in magnetotail-like field reversals: 1. Basic theory of trapped motion. *Journal of*
362 *Geophysical Research Space Physics*, 94(A9), 11821-11842.
363 <https://doi.org/10.1029/JA094iA09p11821>

364 [6] Chandran, B., Li, B., Rogers, B., Quataert, E., & Germaschewski, K. (2010).
365 Perpendicular ion heating by low-frequency Alfvén-wave turbulence in the solar wind.
366 *The Astrophysical Journal*, 720(1). <https://doi.org/10.1088/0004-637X/720/1/503>

367 [7] Chanteur, G. (1998). Spatial interpolation for four spacecraft: Theory. In G.

368 Paschmann, P. W. Daly (Eds.), Analysis methods for multi-spacecraft data (p. 349).
369 Noordwijk, Netherlands: ESA Publ. Div.

370 [8] Chasapis, A., Retinò, A., Sahraoui, F., Vaivads, A., Khotyaintsev, Y. V., Sundkvist,
371 D., Greco, A., Valvo, L. S., & Canu, P. (2015). Thin current sheets and associated
372 electron heating in turbulent space plasma. *The Astrophysical Journal Letters*, 804(1),
373 L1. <https://doi.org/10.1088/2041-8205/804/1/L1>

374 [9] Chen, C. H. K. (2016). Recent progress in astrophysical plasma turbulence from
375 solar wind observations. *Journal of Plasma Physics*, 82(6).
376 <https://doi.org/10.1017/S0022377816001124>

377 [10] Chen, C. H. K., Klein, K. G., & Howes, G. G. (2019). Evidence for electron Landau
378 damping in space plasma turbulence. *Nature communications*, 10(1), 1-8.
379 <https://doi.org/10.1038/s41467-019-08435-3>

380 [11] Dahlin, J. T., Drake, J. F., & Swisdak, M. (2014). The mechanisms of electron
381 heating and acceleration during magnetic reconnection. *Physics of Plasmas*, 21(9),
382 092304. <https://doi.org/10.1063/1.4894484>

383 [12] Dmitruk, P., Matthaeus, W. H., & Lanzerotti, L. J. (2004a). Discrete modes and
384 turbulence in a wave-driven strongly magnetized plasma. *Geophysical Research Letters*,
385 31(21). <https://doi.org/10.1029/2004GL021119>

386 [13] Dmitruk, P., Matthaeus, W. H., & Seenu, N. (2004b). Test particle energization by
387 current sheets and nonuniform fields in magnetohydrodynamic turbulence. *The*
388 *Astrophysical Journal*, 617(1), 667. <https://doi.org/10.1086/425301>

389 [14] Ergun, R. E., Tucker, S., Westfall, J., Goodrich, K. A., Malaspina, D. M., Summers,
390 D., Wallace, J., Karlsson, M., Mack, J., Brennan, N., Pyke, B., Withnell, P., Torbert, R.,
391 Macri, J., Rau, D., Dors, I., Needell, J., Lindqvist, P. -A., Olsson, G., Cully, C. M. (2016).
392 The axial double probe and fields signal processing for the MMS mission. *Space*
393 *Science Reviews*, 199(1), 167–188. <https://doi.org/10.1007/s11214-014-0115-x>

394 [15] Gary, S. P., Winske, D., & Hesse, M. (2000). Electron temperature anisotropy
395 instabilities: Computer simulations. *Journal of Geophysical Research: Space Physics*,
396 105(A5), 10751-10759. <https://doi.org/10.1029/1999JA000322>

397 [16] Greco, A., Matthaeus, W. H., Perri, S., Osman, K. T., Servidio, S., Wan, M., &

398 Dmitruk, P. (2018). Partial variance of increments method in solar wind observations
399 and plasma simulations. *Space Science Reviews*, 214(1), 1-27.
400 <https://doi.org/10.1007/s11214-017-0435-8>

401 [17] Greco, A., Matthaeus, W. H., Servidio, S., Chuychai, P., & Dmitruk, P. (2009).
402 Statistical analysis of discontinuities in solar wind ACE data and comparison with
403 intermittent MHD turbulence. *The Astrophysical Journal*, 691(2), L111.
404 <https://doi.org/10.1088/0004-637X/691/2/L111>

405 [18] He, J., Pei, Z., Wang, L., Tu, C., Marsch, E., Zhang, L., & Salem, C. (2015).
406 Sunward propagating Alfvén waves in association with sunward drifting proton beams
407 in the solar wind. *The Astrophysical Journal*, 805(2), 176. [https://doi.org/10.1088/0004-](https://doi.org/10.1088/0004-637X/805/2/176)
408 [637X/805/2/176](https://doi.org/10.1088/0004-637X/805/2/176)

409 [19] He, J., Wang, L., Tu, C., Marsch, E., & Zong, Q. (2015). Evidence of Landau and
410 cyclotron resonance between protons and kinetic waves in solar wind turbulence. *The*
411 *Astrophysical Journal Letters*, 800(2), L31. [https://doi.org/10.1088/2041-](https://doi.org/10.1088/2041-8205/800/2/L31)
412 [8205/800/2/L31](https://doi.org/10.1088/2041-8205/800/2/L31)

413 [20] Howes, G. G. (2017). A prospectus on kinetic heliophysics. *Physics of Plasmas*,
414 24(5), 055907. <https://doi.org/10.1063/1.4983993>

415 [21] Huang, S. Y., Sahraoui, F., Retinò, A., Le Contel, O., Yuan, Z. G., Chasapis, A.,
416 Aunai, N., Breuillard, H., Deng, X. H., Zhou, M., et al. (2016). MMS observations of
417 ion-scale magnetic island in the magnetosheath turbulent plasma. *Geophysical*
418 *Research Letters*, 43(15), 7850-7858. <https://doi.org/10.1002/2016GL07003>

419 [22] Huang, S. Y., Du, J. W., Sahraoui, F., Yuan, Z. G., He, J. S., Zhao, J. S., Le Contel,
420 O., Breuillard, H., Wang, D. D., Yu, X. D., et al. (2017a). A statistical study of kinetic-
421 size magnetic holes in turbulent magnetosheath: MMS observations. *Journal of*
422 *Geophysical Research: Space Physics*, 122(8), 8577-8588.
423 <https://doi.org/10.1002/2017JA024415>

424 [23] Huang, S. Y., Sahraoui, F., Yuan, Z. G., He, J. S., Zhao, J. S., Le Contel, O., Deng,
425 X. H., Zhou, M., Fu, H. S., Shi, Q.Q., et al. (2017b). Magnetospheric multiscale
426 observations of electron vortex magnetic hole in the turbulent magnetosheath plasma.
427 *The Astrophysical Journal Letters*, 836(2), L27.

428 [8213/aa5f50](https://doi.org/10.3847/2041-8213/aba263)

429 [24] Huang, S. Y., Zhang, J., Sahraoui, F., Yuan, Z. G., Deng, X. H., Jiang, K., Xu, S.
430 B., Wei, Y. Y., He, L. H., & Zhang, Z. H. (2020). Observations of magnetic field line
431 curvature and its role in the space plasma turbulence. *The Astrophysical Journal Letters*,
432 898(1), L18. <https://doi.org/10.3847/2041-8213/aba263>

433 [25] Huang, S. Y., Zhang, J., Yuan, Z. G., Jiang, K., Wei, Y. Y., Xu, S. B., et al. (2022).
434 Intermittent dissipation at kinetic scales in the turbulent reconnection outflow.
435 *Geophysical Research Letters*, 49, e2021GL096403.
436 <https://doi.org/10.1029/2021GL096403>

437 [26] Isenberg, P. A. (2001). The kinetic shell model of coronal heating and acceleration
438 by ion cyclotron waves: 2. Inward and outward propagating waves. *Journal of*
439 *Geophysical Research: Space Physics*, 106(A12), 29249-29260.
440 <https://doi.org/10.1029/2001JA000176>

441 [27] Isenberg, P. A., & Hollweg, J. V. (1983). On the preferential acceleration and
442 heating of solar wind heavy ions. *Journal of Geophysical Research: Space Physics*,
443 88(A5), 3923-3935. <https://doi.org/10.1029/JA088iA05p03923>

444 [28] Kiyani, K. H., Osman, K. T., & Chapman, S. C. (2015). Dissipation and heating in
445 solar wind turbulence: From the macro to the micro and back again. *Philosophical*
446 *Transactions of the Royal Society A: Mathematical, Physical and Engineering Sciences*,
447 373(2041), 20140155. <https://doi.org/10.1098/rsta.2014.0155>

448 [29] Klein, K. G., Howes, G. G., & TenBarge, J. M. (2017). Diagnosing collisionless
449 energy transfer using field-particle correlations: gyrokinetic turbulence. *Journal of*
450 *Plasma Physics*, 83(4). <https://doi.org/10.1017/S0022377817000563>

451 [30] Kress, B. T., Hudson, M. K., Looper, M. D., Albert, J., Lyon, J. G., & Goodrich,
452 C. C. (2007). Global MHD test particle simulations of > 10 MeV radiation belt electrons
453 during storm sudden commencement. *Journal of Geophysical Research: Space Physics*,
454 112(A9). <https://doi.org/10.1029/2006JA012218>

455 [31] Lindqvist, P. A., Olsson, G., Torbert, R. B., King, B., Granoff, M., Rau, D., Needell,
456 G., Turco, S., Dors, I., Beckman, P., et al. (2016). The spin-plane double probe electric
457 field instrument for MMS. *Space Science Reviews*, 199(1), 137-165.

458 <https://doi.org/10.1007/s11214-014-0116-9>

459 [32] Ma, W., Zhou, M., Zhong, Z., & Deng, X. (2020). Electron acceleration rate at
460 dipolarization fronts. *The Astrophysical Journal*, 903(2), 84.
461 <https://doi.org/10.3847/1538-4357/abb8cc>

462 [33] Ma, W., Zhou, M., Zhong, Z., & Deng, X. (2022). Contrasting the Mechanisms of
463 Reconnection-driven Electron Acceleration with In Situ Observations from MMS in the
464 Terrestrial Magnetotail. *The Astrophysical Journal*, 931(2), 135.
465 <https://doi.org/10.3847/1538-4357/ac6be6>

466 [34] Man, H., Zhou, M., Zhong, Z., & Deng, X. (2022). Intense energy conversion
467 events at the magnetopause boundary layer. *Geophysical Research Letters*, 49(8),
468 e2022GL098069. <https://doi.org/10.1029/2022GL098069>

469 [35] Marsch, E., & Tu, C. Y. (2001). Evidence for pitch angle diffusion of solar wind
470 protons in resonance with cyclotron waves. *Journal of Geophysical Research: Space*
471 *Physics*, 106(A5), 8357-8361. <https://doi.org/10.1029/2000JA000414>

472 [36] Matthaeus, W. H., Wan, M., Servidio, S., Greco, A., Osman, K. T., Oughton, S., &
473 Dmitruk, P. (2015). Intermittency, nonlinear dynamics and dissipation in the solar wind
474 and astrophysical plasmas. *Philosophical Transactions of the Royal Society A:*
475 *Mathematical, Physical and Engineering Sciences*, 373(2041), 20140154.
476 <https://doi.org/10.1098/rsta.2014.0154>

477 [37] Osman, K. T., Matthaeus, W. H., Gosling, J. T., Greco, A., Servidio, S., Hnat, B.,
478 Chapman, S. C., & Phan, T. D. (2014). Magnetic reconnection and intermittent
479 turbulence in the solar wind. *Physical Review Letters*, 112(21), 215002.
480 <https://doi.org/10.1103/PhysRevLett.112.215002>

481 [38] Osman, K. T., Matthaeus, W. H., Wan, M., & Rappazzo, A. F. (2012). Intermittency
482 and local heating in the solar wind. *Physical review letters*, 108(26), 261102.
483 <https://doi.org/10.1103/PhysRevLett.108.261102>

484 [39] Pollock, C., Moore, T., Jacques, A., Burch, J., Gliese, U., Saito, Y., Omoto, T.,
485 Avanov, L., Barrie, A., Coffey, V., et al. (2016). Fast plasma investigation for
486 magnetospheric multiscale. *Space Science Reviews*, 199(1), 331-406.
487 <https://doi.org/10.1007/s11214-016-0245-4>

488 [40] Retinò, A., Sundkvist, D., Vaivads, A., Mozer, F., André, M., & Owen, C. J. (2007).
489 In situ evidence of magnetic reconnection in turbulent plasma. *Nature Physics*, 3(4),
490 235-238. <https://doi.org/10.1038/nphys574>

491 [41] Russell, C. T., Anderson, B. J., Baumjohann, W., Bromund, K. R., Dearborn, D.,
492 Fischer, D., Le, G., Leinweber, H. K., Leneman, D., Magnes, W., et al. (2016). The
493 magnetospheric multiscale magnetometers. *Space Science Reviews*, 199(1), 189-256.
494 <https://doi.org/10.1007/s11214-014-0057-3>

495 [42] Sahraoui, F., Goldstein, M. L., Robert, P., & Khotyaintsev, Y. V. (2009). Evidence
496 of a cascade and dissipation of solar-wind turbulence at the electron gyroscale. *Physical*
497 *Review Letters*, 102(23), 231102. <https://doi.org/10.1103/PhysRevLett.102.231102>

498 [43] Vech, D., Klein, K. G., & Kasper, J. C. (2017). Nature of stochastic ion heating in
499 the solar wind: testing the dependence on plasma beta and turbulence amplitude. *The*
500 *Astrophysical Journal Letters*, 850(1), L11. <https://doi.org/10.3847/2041-8213/aa9887>

501 [44] Wang, Y., Bandyopadhyay, R., Chhiber, R., Matthaeus, W. H., Chasapis, A., Yang,
502 Y., Wilder, F. D., Gershman, D. J., Giles, B. L., Pollock, C. J., et al. (2021). Statistical
503 survey of collisionless dissipation in the terrestrial magnetosheath. *Journal of*
504 *Geophysical Research: Space Physics*, 126(6), e2020JA029000.
505 <https://doi.org/10.1029/2020JA029000>

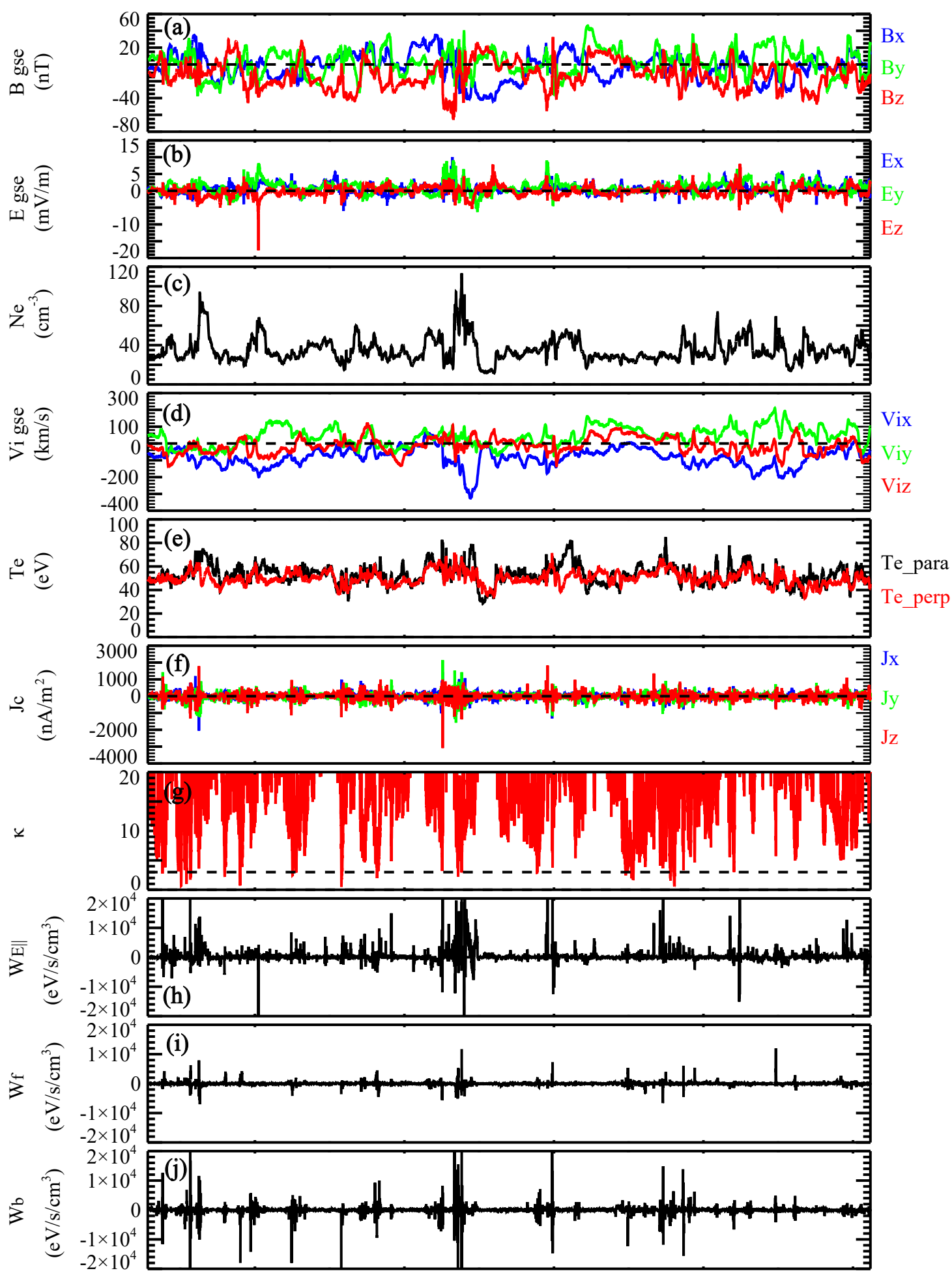
506 [45] Yao, S. T., Shi, Q. Q., Guo, R. L., Yao, Z. H., Tian, A. M., Degeling, A. W., Sun,
507 W. J., Liu, J., Wang, X. G., Zong, Q. G., et al. (2018). Magnetospheric Multiscale
508 observations of electron scale magnetic peak. *Geophysical Research Letters*, 45(2),
509 527-537. <https://doi.org/10.1002/2017GL075711>

510 [46] Zhong, Z. H., Zhou, M., Huang, S. Y., Tang, R. X., Deng, X. H., Pang, Y., & Chen,
511 H. T. (2019). Observations of a kinetic-scale magnetic hole in a reconnection diffusion
512 region. *Geophysical Research Letters*, 46(12), 6248-6257.
513 <https://doi.org/10.1029/2019GL082637>

514 [47] Zhong, Z. H., Zhou, M., Tang, R. X., Deng, X. H., Turner, D. L., Cohen, I. J., Pang,
515 Y., Man, H. Y., Russell, C. T., Giles, B. L., et al. (2020). Direct evidence for electron
516 acceleration within ion-scale flux rope. *Geophysical Research Letters*, 47(1),
517 e2019GL085141. <https://doi.org/10.1029/2019GL085141>

518 [48] Zhou, M., El-Alaoui, M., Lapenta, G., Berchem, J., Richard, R. L., Schriver, D.,
519 & Walker, R. J. (2018). Suprathermal electron acceleration in a reconnecting
520 magnetotail: Large-scale kinetic simulation. *Journal of Geophysical Research: Space*
521 *Physics*, 123(10), 8087-8108. <https://doi.org/10.1029/2018JA025502>
522 [49] Zhou, M., Man, H. Y., Deng, X. H., Pang, Y., Khotyaintsev, Y., Lapenta, G., Yi, Y.
523 Y., Zhong, Z. H., Ma, W. Q. (2021). Observations of secondary magnetic reconnection
524 in the turbulent reconnection outflow. *Geophysical Research Letters*, 48(4),
525 e2020GL091215. <https://doi.org/10.1029/2020GL091215>
526

Figure 1.



mms1 X	11.4	11.4	11.4	11.4	11.4
mms1 Y ^{gse}	0.8	0.8	0.8	0.8	0.8
mms1 Z ^{gse}	0.2	0.2	0.3	0.3	0.3
hhmm	0710	0712	0714	0716	0718
2016 Dec 18					

Figure 2.

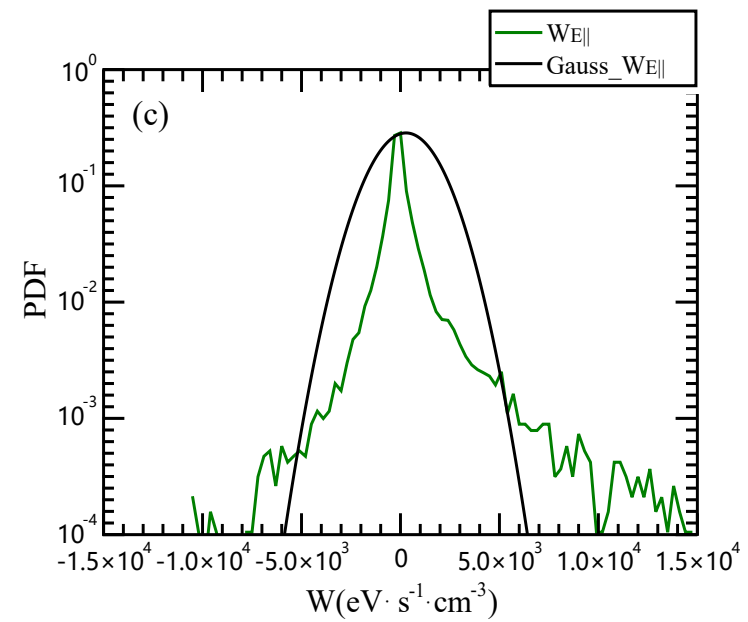
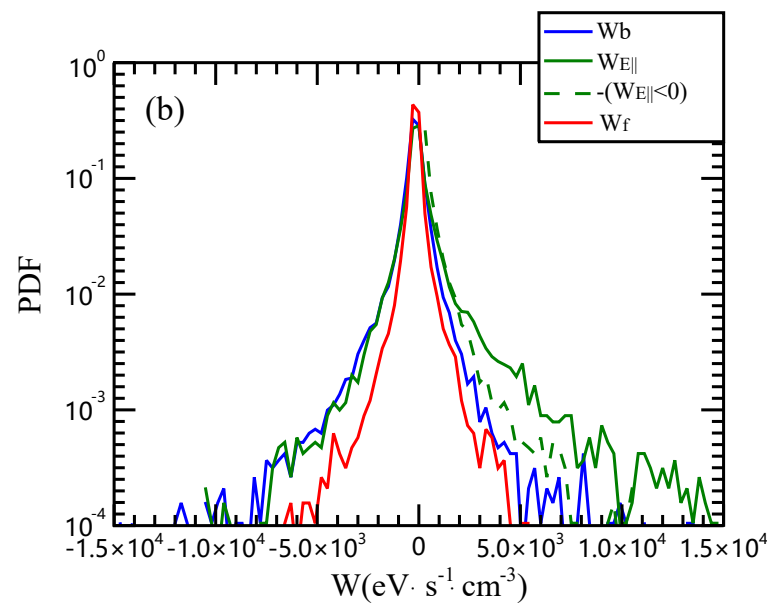
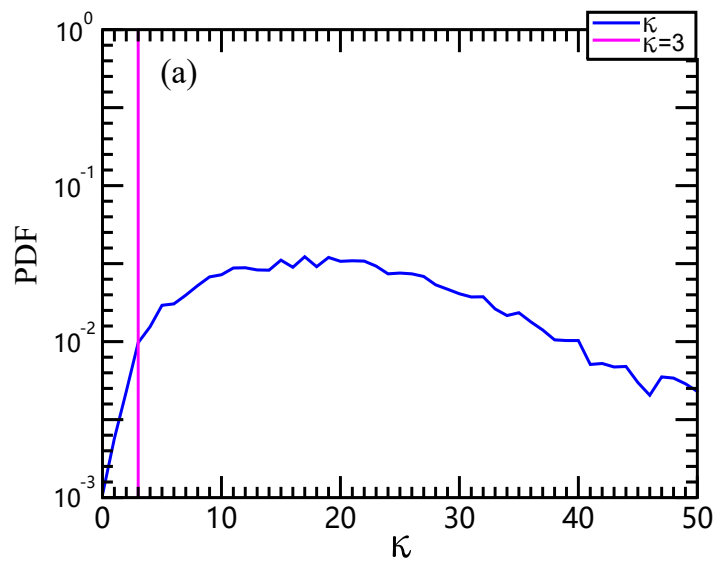


Figure 3.

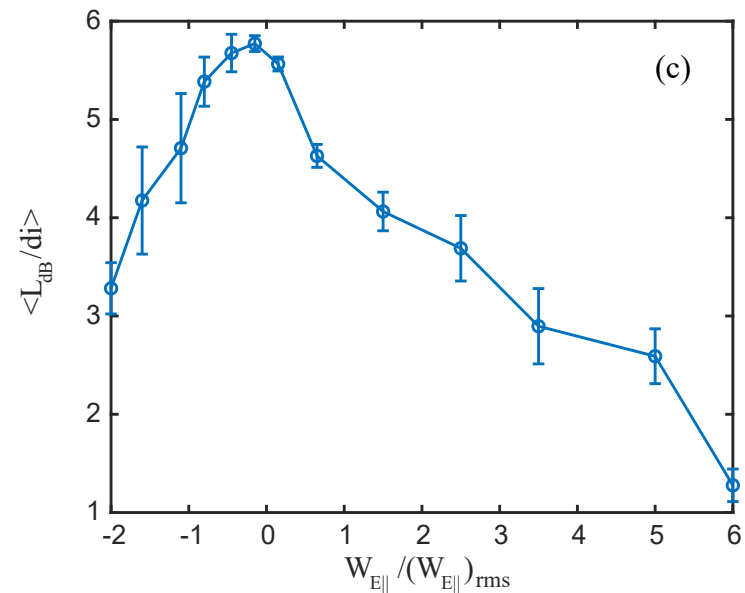
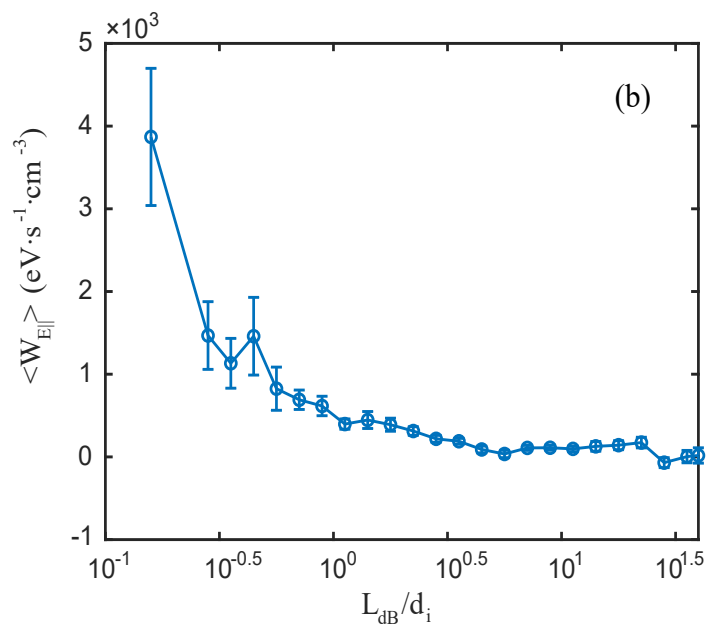
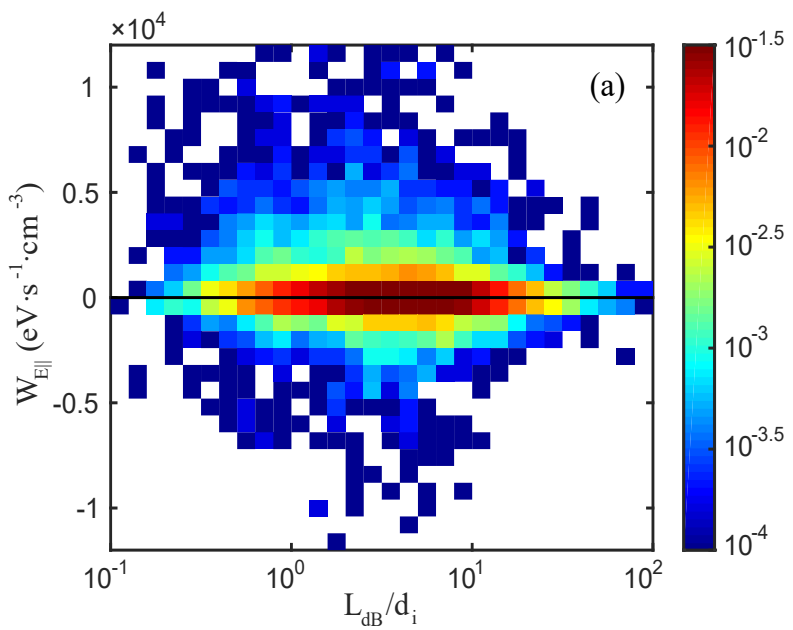


Figure 4.

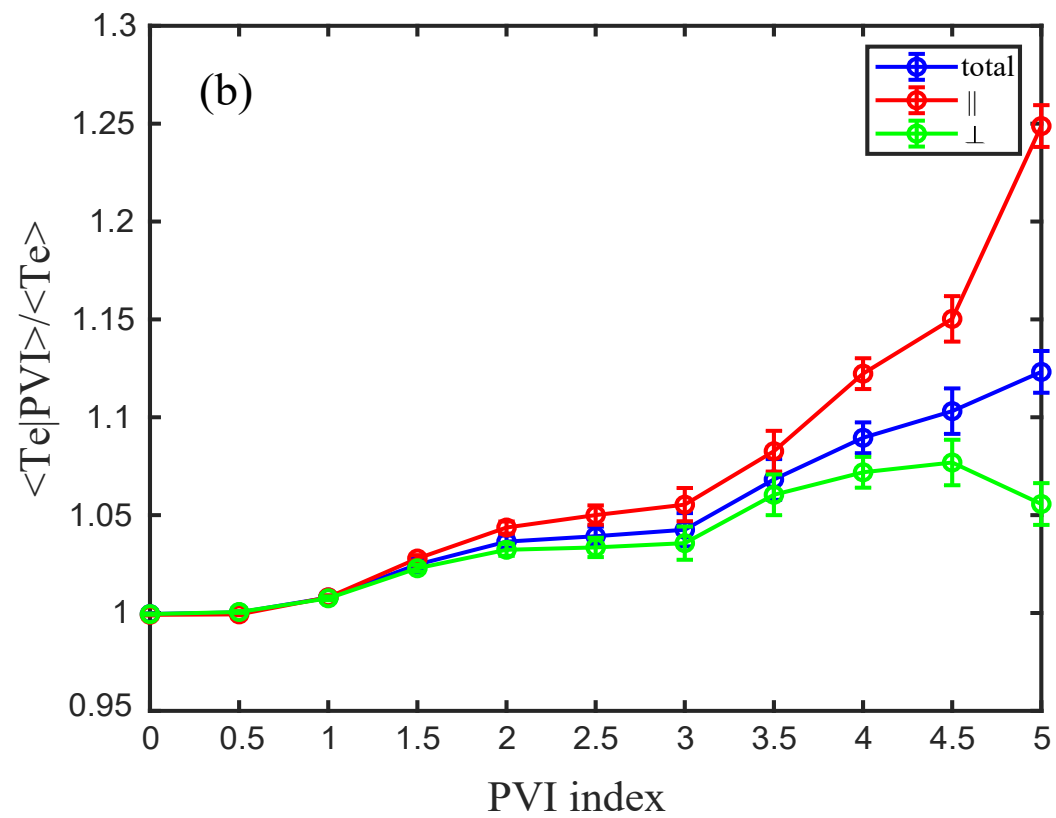
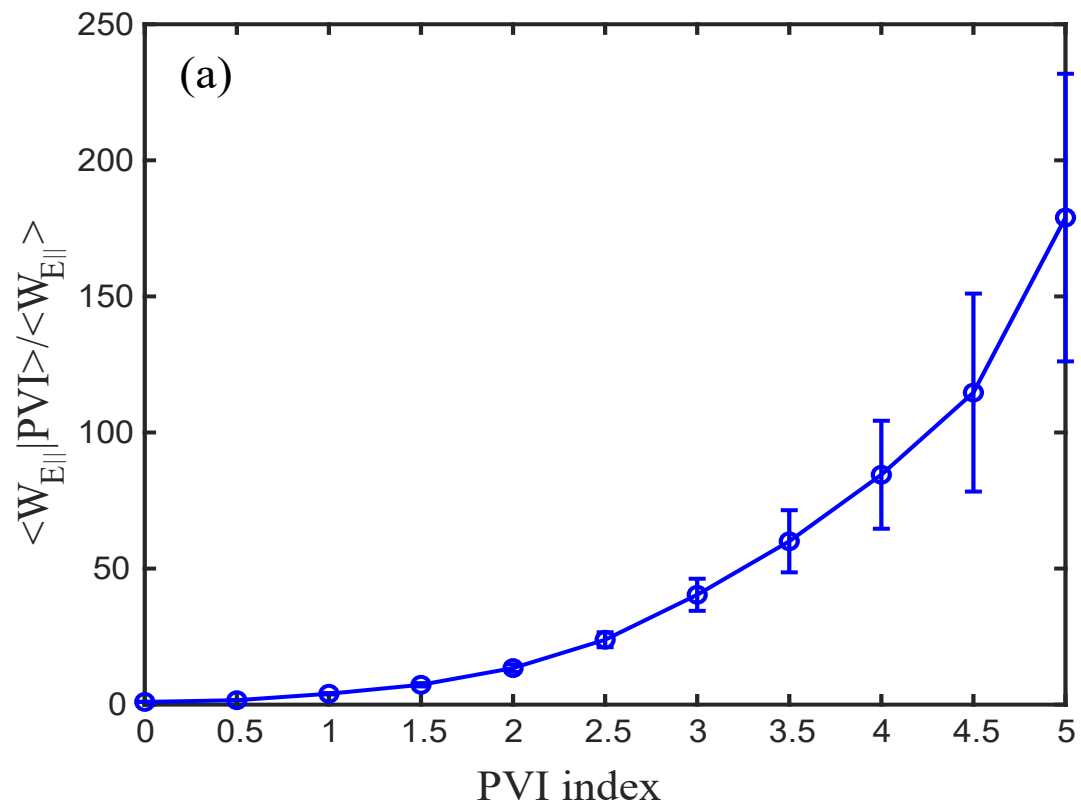
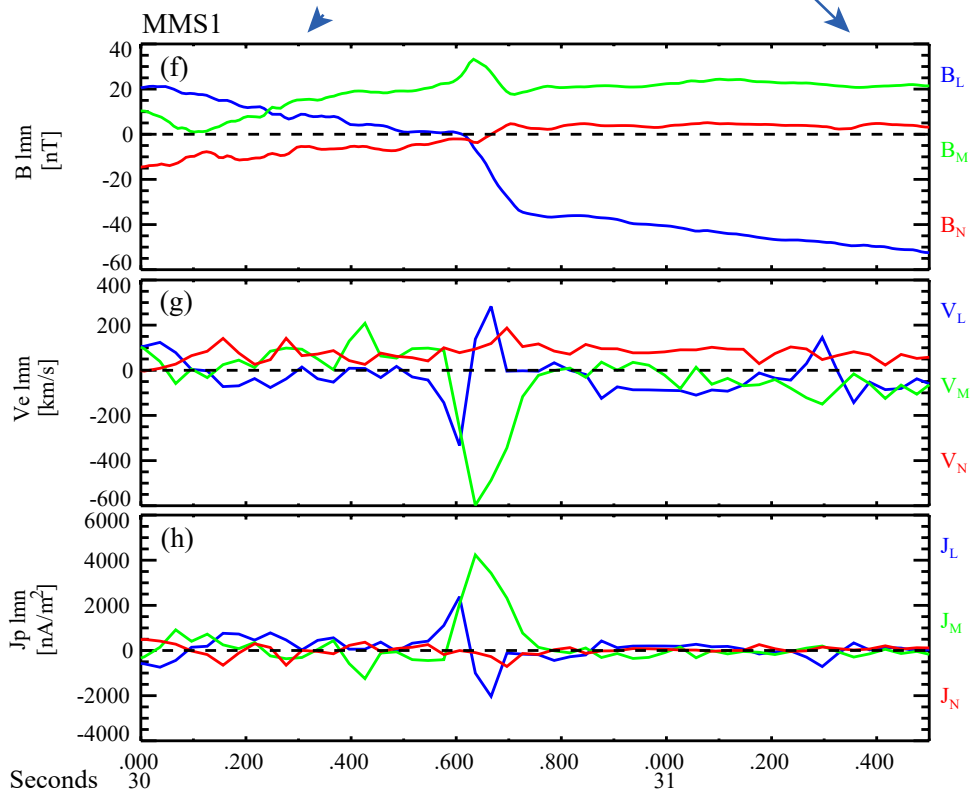
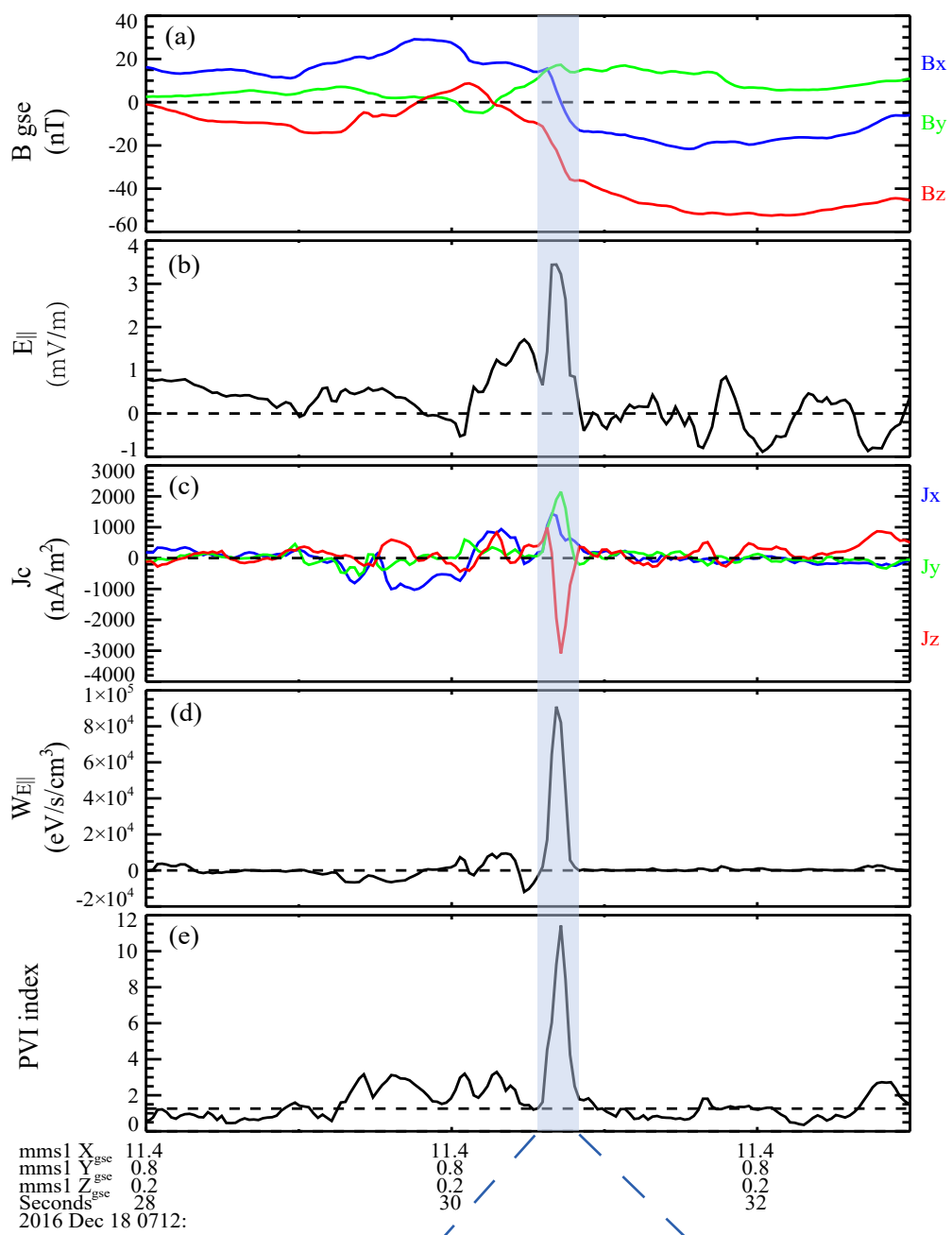


Figure 5.



1 **Electron Heating in Magnetosheath Turbulence: Dominant Role of** 2 **the Parallel Electric Field within Coherent Structures**

3 Qianyun Xu^{1,2}, Meng Zhou^{1,2}, Wenqing Ma², Jiansen He³,
4 Shiyong Huang⁴, Zhihong Zhong^{1,2}, Ye Pang², Xiaohua Deng²

5
6 1. Department of Physics, School of Physics and Materials Science, Nanchang
7 University, Nanchang 330031, People's Republic of China;

8 2. Institute of Space Science and Technology, Nanchang University, Nanchang
9 330031, People's Republic of China;

10 3. School of Earth and Space Sciences, Peking University, Beijing 100871, People's
11 Republic of China;

12 4. School of Electronic Information, Wuhan University, Wuhan, People's Republic
13 of China;

14 **Key points:**

- 15 1. Electrons are primarily accelerated by the parallel electric field in the
16 magnetosheath turbulence.
17 2. The E_{\parallel} acceleration mostly occurs within the coherent structures through Joule-type
18 dissipation.
19 3. The average E_{\parallel} acceleration rate increases with the decreasing local spatial scale.

20 **Abstract**

21 How are particles being energized by turbulent electromagnetic fields is an
22 outstanding question in plasma physics and astrophysics. This paper investigates the
23 electron acceleration mechanism in strong turbulence ($\delta B/B_0 \sim 1$) in the Earth's
24 magnetosheath based on the novel observations of the Magnetospheric Multiscale
25 (MMS) mission. We find that electrons are magnetized in turbulent fields for the
26 majority of the time. By directly calculating the electron acceleration rate from Fermi,
27 betatron mechanism, and parallel electric field, it is found that electrons are primarily
28 accelerated by the parallel electric field within coherent structures. Moreover, the
29 acceleration rate by parallel electric fields increases as the spatial scale reduces, with

30 the most intense acceleration occurring over about one ion inertial length. This study is
31 an important step towards fully understanding the turbulent energy dissipation in
32 weakly collisional plasmas.

33 **Plain language summary**

34 The magnetosheath is one of the most turbulent environments in near-Earth space,
35 which is very beneficial to the study of collisionless turbulent plasma. The mechanism
36 of turbulent energy dissipation and the consequent plasma heating is not fully
37 understood. The Magnetosphere Multiscale mission provides high-time cadence data
38 and simultaneous multi-spacecraft measurements at very small inter-spacecraft
39 separations. That can measure important quantities related to dissipation and heating at
40 kinetic scales. This paper investigates how electrons are being accelerated through the
41 dissipation of magnetic energy in nonlinear turbulence in the Earth's magnetosheath.
42 We classify the acceleration mechanisms into three types: Fermi mechanism, betatron
43 mechanism, and E_{\parallel} acceleration. By directly calculating and comparing these
44 mechanisms, we find electrons are predominantly accelerated by parallel electric fields
45 within coherent structures. The E_{\parallel} acceleration is the most effective around the ion
46 inertial length.

47

48 **1. Introduction**

49 Energy cascade is one of the most prominent features of turbulence. Energy is
50 injected at large scales, like fluid scales, then cascades to small scales through non-
51 linear interactions, and finally dissipated at kinetic scales, leading to plasma heating
52 and particle acceleration and the formation of suprathermal tails in the particle energy
53 spectrum (Kiyani et al., 2015). Space plasma is typical of weak collisionality; hence
54 collisionless mechanisms play a critical role in turbulent energy dissipation in space
55 plasmas (Matthaeus et al., 2015; Chen 2016; Howes 2017). How the particles are
56 heated/accelerated by turbulence is one of the most outstanding questions in plasma
57 turbulence; however, the mechanism of turbulent energy dissipation and the consequent
58 plasma heating is not fully understood after decades of intensive study.

59 Different types of acceleration mechanisms have been proposed to explain plasma

60 heating by the turbulent cascade in collisionless plasma. These mechanisms can be
61 generally classified into two categories: resonant acceleration and non-resonant
62 acceleration. The dissipation of waves is usually due to the energy transfer to energizing
63 particles caused by field and particle resonance, which can work over a long distance
64 and a long time. It includes Landau damping, cyclotron damping, and transit-time
65 damping (Chandran et al., 2010; Dmitruk et al., 2004a; Sahraoui et al., 2009; Isenberg
66 & Hollweg 1983; Gary et al., 2000; Isenberg 2001; Marsch & Tu 2001; Klein et al.,
67 2017). Previous studies have found clues of this resonant acceleration in space plasma
68 turbulence. He et al. (2015a, 2015b) suggested that solar wind ions are heated by
69 Landau damping and cyclotron damping by identifying characteristic signatures of
70 these resonances in the ion velocity distribution functions. Recently, in situ signature of
71 cyclotron resonant heating in the solar wind turbulence is observed by Parker Solar
72 Probe observations (Bowen et al., 2022). Chen et al. (2019) presented direct evidence
73 for Landau damping in magnetosheath turbulence by using the novel field-particle
74 correlation technique. The Landau damping mechanism for electron heating is further
75 confirmed by examining more events in the magnetosheath using the same field-particle
76 correlation method (Afshari et al., 2021).

77 One typical non-resonant acceleration is stochastic heating, which heats plasma
78 when the motion of particles becomes chaotic as the amplitude of electromagnetic field
79 fluctuations, at scales comparable to the gyro-scale, exceeds a critical value (Chandran
80 et al., 2010; Vech et al., 2017). It is found that acceleration and dissipation also occur
81 in coherent structures, such as current sheets (Retinò et al., 2007; Dmitruk et al., 2004b;
82 Osman et al., 2012), magnetic islands (Huang et al., 2016), small-scale vortices
83 (Alexandrova & Saur 2008), and magnetic holes (Huang et al., 2017a, 2017b; Zhong et
84 al., 2019), etc. It is suggested that magnetic reconnection occurring within the current
85 sheets in turbulence provides an important pathway for energy dissipation (Osman et
86 al., 2014; Zhou et al., 2021). The correlation between energy dissipation and localized
87 coherent structures indicates that energy dissipation may occur non-uniformly.

88 The motivation of this study is to investigate the acceleration and heating of electrons
89 in plasma turbulence. Different from Chen et al. (2019) and Afshari et al. (2021), the

90 turbulent interval we examine in this paper has large fluctuations with $\delta B/B_0 \sim 1$. In
 91 addition, we not only quantify the electron acceleration rate by the parallel electric field,
 92 as has been done by Chen et al. (2019) and Afshari et al. (2021), but also quantify the
 93 acceleration by the perpendicular electric field. The electron acceleration rates are
 94 evaluated under the guiding center approximation. We have used the data from the
 95 Magnetospheric Multiscale (MMS) mission, which provides high-time cadence data
 96 and simultaneous multi-spacecraft measurements at very small inter-spacecraft
 97 separations. This combination enables the study of the nature of dissipation at kinetic
 98 scales with an unprecedented level of accuracy and resolution. The FGM magnetic field
 99 instruments (Russell et al., 2016), EDP electric field instruments (Ergun et al., 2016;
 100 Lindqvist et al., 2016), and FPI ion and electron detectors (Pollock et al., 2016) provide
 101 the high-resolution data required to characterize signatures of dissipation and heating.

102

103 **2. Methodology**

104 Here we employ the method that has been used to calculate the acceleration rate in
 105 reconnection. This method considers the particle energy gain under guiding center
 106 approximation (Dahlin et al., 2014; Zhou et al., 2018; Zhong et al., 2020; Ma et al.,
 107 2020, 2022). The integrated energy gain of electrons in a unit volume per unit time for
 108 betatron acceleration is given by:

$$109 \quad W_b = P_{e\perp} \mathbf{v}_{E \times B} \cdot \frac{\nabla \mathbf{B}}{B} + \frac{P_{e\perp}}{B} \frac{\partial B}{\partial t} \quad (1)$$

110 where $P_{e\perp}$ is the perpendicular electron pressure, $\mathbf{v}_{E \times B}$ is the $E \times B$ drift speed, $\nabla \mathbf{B}$ is
 111 the gradient of the total magnetic field. We refer to W_b as the betatron acceleration
 112 rate hereafter. Betatron acceleration might be efficient in magnetosheath turbulence,
 113 which usually involves large-amplitude $|B|$ fluctuations, such as magnetic holes and
 114 magnetic peaks (e.g., Huang et al., 2017a, 2017b; Yao et al., 2018).

115 The Fermi acceleration rate is calculated by

$$116 \quad W_f = (P_{e\parallel} + n_e m_e v_{e\parallel}^2) \mathbf{v}_{E \times B} \cdot (\mathbf{b} \cdot \nabla \mathbf{b}) \quad (2)$$

117 where $P_{e\parallel}$ is the electron parallel pressure, $v_{e\parallel}$ is the electron parallel bulk velocity and
 118 \mathbf{b} is the unit vector of the magnetic field. Fermi acceleration is essentially caused by the

119 curvature drift in motional curved field lines. In situ observations in the magnetosheath
 120 suggest that curvature drift acceleration may be important for particle energization in
 121 magnetized turbulence (Bandyopadhyay et al., 2020; Huang et al., 2020).

122 The E_{\parallel} acceleration rate, which is caused by the parallel electric field, is given by

$$123 \quad W_{E_{\parallel}} = J_{e\parallel} E_{\parallel} + \frac{\beta_{e\perp}}{2} J_{\parallel} E_{\parallel} \quad (3)$$

124 where $\beta_{e\perp}$ is the ratio between the perpendicular electron pressure and the magnetic
 125 pressure, J_{\parallel} is the total parallel current density and $J_{e\parallel}$ is the parallel current carried by
 126 electrons. The presence of $\frac{\beta_{e\perp}}{2} J_{\parallel} E_{\parallel}$ is to eliminate the work caused by the parallel
 127 magnetization drift.

128 Betatron and Fermi mechanisms cause the heating of plasmas while E_{\parallel} leads to not
 129 only plasma heating but also plasma bulk acceleration. The heating of plasma by E_{\parallel} can
 130 be understood by examining the electron momentum equation:

$$131 \quad E_{\parallel} = -\frac{1}{en} (\nabla \cdot \mathbf{P}_e)_{\parallel} - \frac{m_e}{e} \left(\frac{dv_e}{dt} \right)_{\parallel} \quad (4)$$

132 where e is the unit charge, n is the number density, v_e is the electron bulk velocity and
 133 \mathbf{P}_e is the electron pressure tensor. The relationship between the parallel electric field
 134 and the electron energy gain can be obtained by multiplying Eq. (4) by $-nev_{e\parallel}$:

$$135 \quad -nev_e E_{\parallel} = v_{e\parallel} (\nabla \cdot \mathbf{P}_e)_{\parallel} + nm_e v_{e\parallel} \left(\frac{dv_e}{dt} \right)_{\parallel} \quad (5)$$

136 The first term on the RHS of Eq. (5) contributes to the thermal energy increase of
 137 electrons, i.e., electron heating, while the second term on the RHS of Eq. (5) is related
 138 to the electron bulk velocity variation.

139 Equations (1) – (3) can be used to evaluate the acceleration rates for the three
 140 different types of mechanisms when the electrons satisfy the guiding center
 141 approximation, i.e., they are magnetized, or say, the 1st adiabatic invariant is conserved.
 142 To test this criterion, we calculate κ (Büchner & Zelenyi 1989):

$$143 \quad \kappa_{\text{curv}} = \sqrt{R_c / \rho_e} \quad (6)$$

144 where R_c is the curvature radius of the magnetic field, and ρ_e is the electron gyration
 145 radius, which is calculated by using four times the electron temperature, higher than the
 146 energy of most electrons in the magnetosheath. When $\kappa > 3$, electrons of the specific

147 energy are considered to satisfy the guiding center approximation. In the following
148 study, we calculate the acceleration rates only at times when κ is greater than 3.

149

150 **3. Results**

151 Figure 1 shows the overview of the MMS observations in a turbulent magnetosheath
152 from 07:08:14 to 07:18:34 UT on 2016 December 18. The location of the MMS
153 spacecraft in the geocentric solar ecliptic (GSE) coordinate system is [11.4, 0.8, 0.2] R_E
154 (R_E is earth radii), downstream of the quasi-perpendicular bow shock. The average
155 spacing of the MMS tetrahedron is $\sim 8.5 \text{ km} \sim 9.5 d_e$ given the average plasma density
156 of $\sim 35 \text{ cm}^{-3}$, where d_e is the electron inertial length. The tetrahedron quality factor (TQF)
157 is ~ 0.99 , indicating that the four satellites constitute a nearly perfect tetrahedron in
158 space. One can see from Figures 1a-1c that the electromagnetic fields and plasma flows
159 are highly turbulent. The electron flow speed is similar to that of the ion flow, except
160 that electron bulk velocity has some high-frequency fluctuations, which leads to
161 filamentary currents with peak density larger than 500 nA m^{-2} (Figure 1f). The electron
162 temperature exhibits an anisotropy with $T_{e\parallel} > T_{e\perp}$ in this interval (Figure 1g). The average
163 ion bulk velocity is about 120 km s^{-1} and the average electron temperature is about 50
164 eV.

165 Figure 1g shows that κ is larger than 3 (the black dotted line) for most of the time.
166 This can be also clearly seen in the probability distribution function (PDF) of the κ
167 values displayed in Figure 2a. About 99% of κ are greater than 3, which means that
168 electrons are magnetized almost during the entire interval. The PDF of κ increases from
169 nearly 0 and reaches the peak at around $\kappa=18$, then it monotonically descends as the
170 increment of κ . Figures 1h-1j display the electron acceleration rates for the three
171 different acceleration mechanisms. They have both positive and negative values,
172 suggesting bi-directional energy exchange between the electromagnetic fields and
173 electrons rather than unidirectional energy conversion. The largest acceleration rate is
174 up to $2 \times 10^4 \text{ eV s}^{-1} \text{ cm}^{-3} \sim 3.2 \text{ nW m}^{-3}$. There are many spikes in accelerated rates, which
175 is the manifestation of intermittency. Note that the above three acceleration rates are

176 calculated in the frame co-moving with the magnetosheath flow, that is, $\mathbf{E}' = \mathbf{E} + \langle \mathbf{V} \rangle \times$
177 \mathbf{B} , where $\langle \mathbf{V} \rangle$ is the average ion bulk velocity in the whole interval.

178 To determine the main acceleration mechanism, we plot the PDF of the three
179 acceleration rates in Figure 2b. The total number of data points is about 20,000. We see
180 that the highest value of the PDF is around $W=0$. The PDFs are sign-indefinite, which
181 implies that the energy exchange between electromagnetic fields and plasmas goes both
182 ways. The PDF of $W_{E_{\parallel}}$ is the broadest among the three, indicating that E_{\parallel} acceleration
183 is generally greater than the other two mechanisms. The PDF of $W_{E_{\parallel}}$ is asymmetric with
184 respect to $W=0$, with a higher positive tail, while the PDF of W_b shows a subtle heavier
185 negative tail and the PDF of W_f is nearly symmetric to $W=0$. The average acceleration
186 rate of E_{\parallel} , betatron, and Fermi acceleration is $278 \text{ eV s}^{-1} \text{ cm}^{-3}$, $-77 \text{ eV s}^{-1} \text{ cm}^{-3}$, and -4
187 $\text{eV s}^{-1} \text{ cm}^{-3}$, respectively. Therefore, on average, electrons were accelerated by E_{\parallel} ,
188 whereas betatron and Fermi mechanisms decelerated the electrons. The average
189 energization rate of electrons by E_{\parallel} is at least one order of magnitude larger than the
190 results reported in previous literature (Afshari et al., 2021; Bandyopadhyay et al., 2020).
191 The PDF of $W_{E_{\parallel}}$ is non-Gaussian with a heavier tail (Figure 2c), suggesting the
192 intermittent nature of the acceleration process (Matthaeus et al., 2015). The
193 intermittency is further proved by the large kurtosis of the E_{\parallel} , betatron, and Fermi
194 acceleration rate, which is 374, 196, and 72, respectively.

195 Since the acceleration of electrons is dominated by parallel electric fields, we mainly
196 focus on E_{\parallel} acceleration in the following. To understand at which scale the acceleration
197 occurs, we estimate the spatial scale of the magnetic field $L_{dB} = B/|\nabla \mathbf{B}|$ using the
198 multi-spacecraft measurements under the assumption that the spatial variation is linear
199 inside the MMS tetrahedron (Chanteur 1998). Here, $|\nabla \mathbf{B}|$ is the norm of the Jacobian
200 matrix of the magnetic field, i.e., $|\nabla \mathbf{B}| = \sqrt{\sum_{ij} (\frac{\partial B_i}{\partial x_j})^2}$ (Kress et al. 2007). Figure 3a
201 shows the joint PDF of the E_{\parallel} acceleration rate $W_{E_{\parallel}}$ and the L_{dB} . We see that most of the
202 data points are near $W_{E_{\parallel}}=0$, which is consistent with Figure 2b. L_{dB} is typically larger
203 than $\sim 0.3 d_i$ and smaller than $30 d_i$. Figure 3b points out that the average acceleration
204 rate descends with the increment of the spatial scale, from larger than $1000 \text{ eV s}^{-1} \text{ cm}^{-3}$

205 when $L_{dB} < 10^{-0.5} d_i$ to less than $200 \text{ eV s}^{-1} \text{ cm}^{-3}$ when $L_{dB} > 10 d_i$. Figure 3c displays
 206 that the average L_{dB} is the largest near $W_{E||}=0$ and descends toward larger $W_{E||}$ in both
 207 the positive and negative directions. The average L_{dB} reduces to about $1 d_i$ when $W_{E||}$ is
 208 6 times larger than its RMS.

209 The Partial Variance of Increments (PVI) method has been widely used to identify
 210 the coherent structures in turbulent plasma (Matthaeus et al., 2015; Greco et al., 2009,
 211 2018; Chasapis et al., 2015). The PVI index can be calculated using magnetic fields
 212 observed by multi-spacecraft:

$$213 \quad PVI_{ij}(t) = \sqrt{\frac{|B^i(t) - B^j(t)|^2}{\langle |B^i(t) - B^j(t)|^2 \rangle}} \quad (7)$$

214 where the subscript $i, j=1,2,3,4$ indicates the different spacecraft. Figure 4a shows the
 215 $E_{||}$ acceleration rate conditioned on the PVI index. We see that the average $W_{E||}$
 216 monotonically increases with the increment of PVI index, which means that the most
 217 intense $E_{||}$ acceleration corresponds to the largest PVI index. The average $W_{E||}$ with PVI
 218 index >3 is about 40 times the $W_{E||}$ averaged over all the data points. We also examine
 219 the local increase of the electron temperature conditioned on the PVI index (Figure 4b).
 220 The local increase of the electron temperature is represented by the electron temperature
 221 normalized by its regional average. It shows that similar to the profile of $W_{E||}$, the
 222 average T_e also increases nearly monotonically with the increase of the PVI index.
 223 Notice that the monotonic trend is clearer in $T_{e||}$ than in $T_{e\perp}$. This is consistent with
 224 previous observations that strong electron heating, measured by the local increase of
 225 the electron temperature, occurs within current sheets with large PVI index, while no
 226 apparent heating within current sheets with small PVI index (Chasapis et al., 2015;
 227 Huang et al., 2022). Here we go one step further by confirming that structures with
 228 larger PVI index contribute to greater energy dissipation and electron acceleration.

229 Moreover, we investigate where the most intense $E_{||}$ acceleration occurs. We define
 230 the intense $E_{||}$ acceleration event as the interval in which the peak $W_{E||}$ is greater than
 231 $5,100 \text{ eV s}^{-1} \text{ cm}^{-3}$. This value is the intersection of the PDF of $W_{E||}$ and the Gaussian
 232 curve in Figure 2c. The boundary of each event is set as $5100/e \approx 1,900$, where e is the

233 natural exponential. We identify the coherent structures when the PVI index is larger
234 than the threshold $\langle PVI \rangle + \sigma(PVI) \sim 1.3$, where $\langle PVI \rangle$ and $\sigma(PVI)$ are the average and
235 standard deviation of PVI index in the entire interval (Greco et al., 2009). Finally, 68
236 intense E_{\parallel} acceleration events were selected, with 60 events having a PVI index greater
237 than the threshold, i.e., they are within the coherent structures. One can see from Figure
238 3a that data points with $W_{E_{\parallel}}$ larger than $5,100 \text{ eV s}^{-1} \text{ cm}^{-3}$ are mostly in the range $L_{\text{dB}} \sim$
239 $[1, 10] \text{ d}_i$.

240 Figure 5 shows one example of intense E_{\parallel} acceleration events. It is shown that the
241 intense E_{\parallel} acceleration was coincident with a large PVI index, which corresponds to a
242 coherent structure with a sharp change of the magnetic field and an intense current. A
243 unipolar $E_{\parallel} \sim 3 \text{ mV m}^{-1}$ was responsible for $\sim 8 \times 10^4 \text{ eV s}^{-1} \text{ cm}^{-3}$ acceleration rate in the
244 parallel direction. Moreover, we transfer the magnetic field, electron bulk flow, and
245 electric current to the local LMN coordinates (Figure 5g-5i) to see whether this event
246 was associated with a local reconnection. We employ the same procedure as Man et al.
247 (2022) to identify local reconnection, such as the electron outflowing jets and the out-
248 of-plane current supporting the magnetic field reversal. We see a clear electron bulk
249 flow reversal corresponding well to the current sheet crossing, implying that MMS
250 encountered an active reconnection in this coherent structure. We have further
251 examined all the intense E_{\parallel} acceleration events. Overall, 30 ($\sim 44\%$) intense E_{\parallel}
252 acceleration events are associated with local reconnection. Therefore, we conclude that
253 reconnection plays a significant role in accelerating electrons in this event.

254

255 **4. Discussion and Conclusion**

256 We have analyzed 31 other intervals in the turbulent magnetosheath observed by
257 MMS from the year 2015 to 2019 (Wang et al., 2021). Twenty-two of these intervals
258 are downstream of the quasi-parallel bow shock, and the other 9 events are downstream
259 of the quasi-perpendicular bow shock. These events have a broader range of plasma β .
260 We analyze these events by the same method described in this paper and find
261 qualitatively similar results, that is, electrons are predominantly accelerated by E_{\parallel} no

262 matter whether the interval is downstream of the quasi-parallel or quasi-perpendicular
263 bow shock.

264 A further question that needs to be addressed is whether the E_{\parallel} acceleration in the
265 coherent structures is due to Landau damping, stochastic heating, or Joule-type
266 dissipation. Since the electrons are magnetized most of the time, they could not be
267 energized through stochastic heating, which requires that the electron magnetic moment
268 is not conserved (e.g., Vech et al., 2017). This event is different from the events reported
269 by Afshari et al. (2021) and Chen et al. (2019), which demonstrate that electrons were
270 accelerated through Landau resonance with the kinetic Alfvén waves. One major
271 difference is that the magnetic field is relatively stable and has few coherent structures
272 in the events studied by Afshari et al. (2021). This is also manifested by the non-
273 Gaussian PDF of the E_{\parallel} acceleration rate in our event, whereas the PDF is near Gaussian
274 in turbulence dominated by Landau damping (not shown). Importantly, we find that the
275 large E_{\parallel} acceleration studied in this paper is usually associated with unipolar E_{\parallel} rather
276 than wave-like E_{\parallel} . Thus, the E_{\parallel} acceleration observed in our event is unlikely caused by
277 Landau damping. More detailed analysis using the field-particle correlation technique
278 for each intense E_{\parallel} acceleration event can be performed to further understand E_{\parallel}
279 acceleration in these coherent structures.

280 In summary, we have investigated how electrons are being accelerated through the
281 dissipation of magnetic energy in nonlinear turbulence in the Earth's magnetosheath.
282 Since electrons are mostly magnetized, we classify the acceleration mechanisms into
283 three types: Fermi process, betatron mechanism, and E_{\parallel} acceleration. We find that the
284 PDF of E_{\parallel} acceleration is significantly broader than the PDF of the other two
285 acceleration rates, which implies that electrons are predominantly accelerated by
286 parallel electric fields. $W_{E_{\parallel}}$ increases with the reduction of the spatial scale and the
287 increment of the PVI index, suggesting that the E_{\parallel} acceleration is the most effective
288 around the ion inertial length and coherent structures play a vital role in energizing
289 electrons through E_{\parallel} . We demonstrate that electrons are accelerated through Joule-type
290 dissipation/heating in strong turbulence containing many coherent structures, which is
291 another important building block of the particle energization physical scenario besides

292 the mechanism proposed by Chen et al. (2019) and Afshari et al. (2021).

293 The acceleration and heating of ions by turbulence may be quite different to the
294 electrons because ions are expected to be demagnetized due to their much larger gyro-
295 radius. Hence one cannot use the guiding center approximation to describe the ion
296 motion and may resort to other methods to quantify the ion acceleration, which is
297 underway for further report.

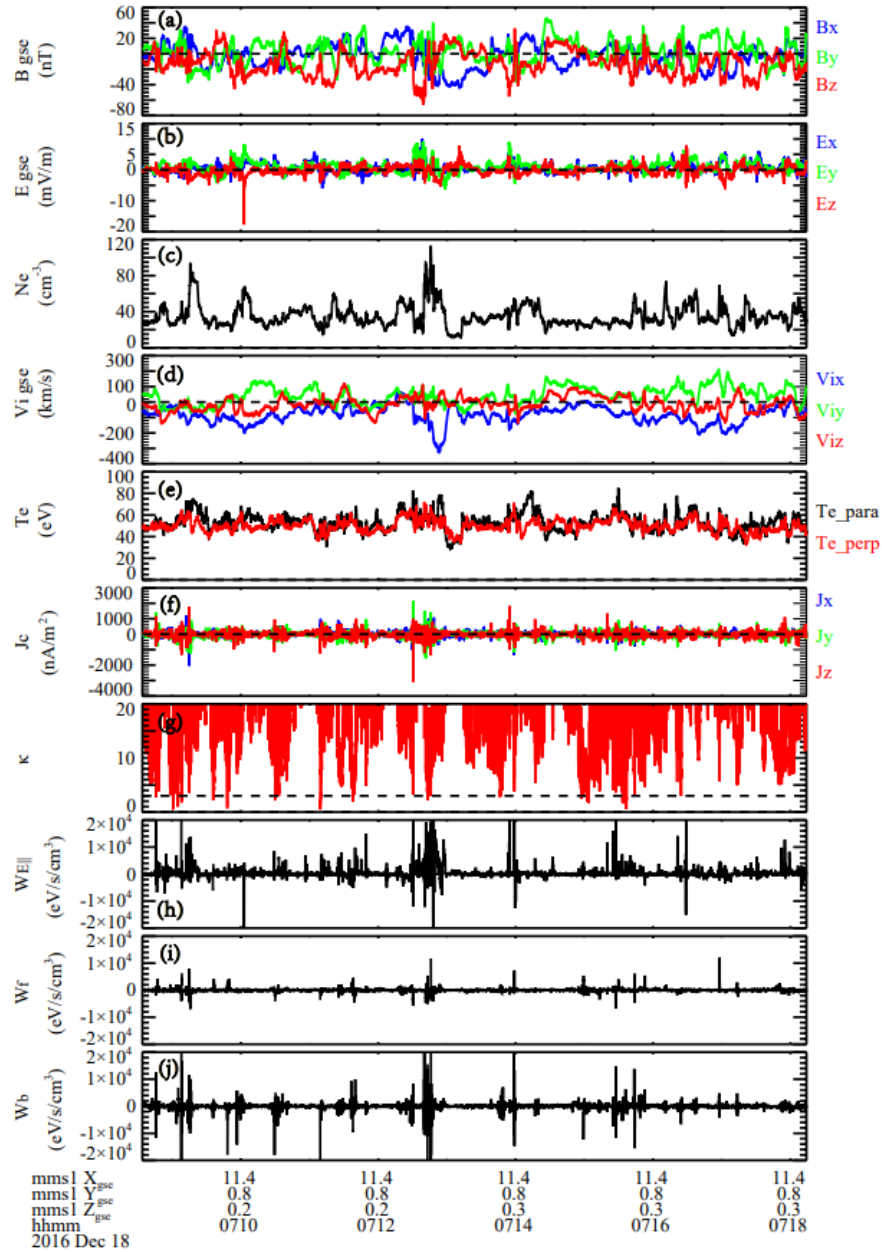
298

299 **Acknowledgments**

300 Thanks to the MMS team for providing the high-quality data to complete this work.
301 This work is supported by the National Natural Science Foundation of China (NSFC)
302 under grant Nos. 42074197, 42130211, and 41774154.

303 **Data Availability Statement**

304 The data used in this study was obtained from the MMS Science Data Center
305 (<https://lasp.colorado.edu/mms/sdc/public/about/browse-wrapper/>).

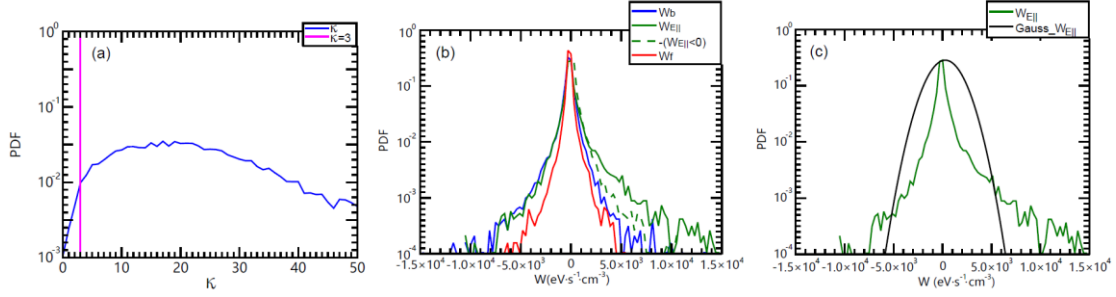


306

307 **Figure 1.** Overview of the turbulence in the magnetosheath observed by MMS from
 308 07:08:14 to 07:18:34 UT on 18 December 2016. From the top to bottom are: (a) three
 309 components of the magnetic field and (b) the electric field; (c) electron number density;
 310 (d) ion bulk velocity; (e) electron parallel and perpendicular temperatures; (f) electric
 311 current density; (g) κ value; (h) – (j) the acceleration rate from E_{\parallel} , Fermi process and
 312 betatron mechanism, respectively. The vectors are displayed in the GSE coordinate
 313 system.

314

315



316

317 **Figure 2.** (a) probability distribution function (PDF) of κ . The pink line marks $\kappa=3$; (b)

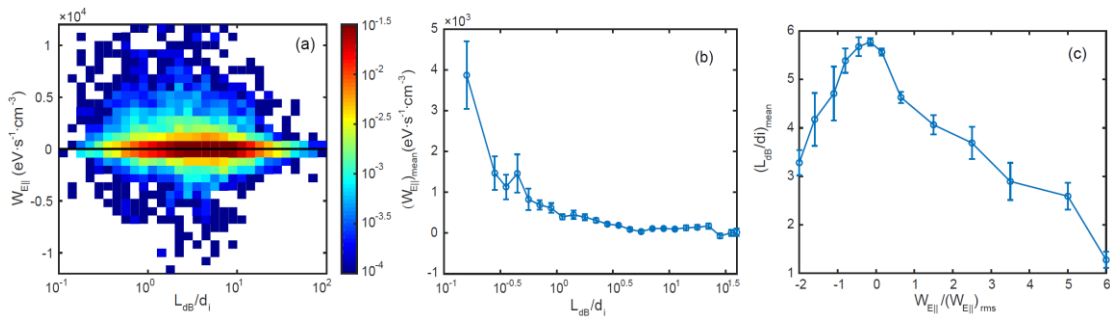
318 PDF of betatron acceleration rate (blue), Fermi acceleration rate (red) and the E_{\parallel}

319 acceleration rate (green). The green dashed line is the mirror image of the negative E_{\parallel}

320 acceleration rate; (c) comparison of the PDF of the E_{\parallel} acceleration rate and the Gaussian

321 curve (black).

322



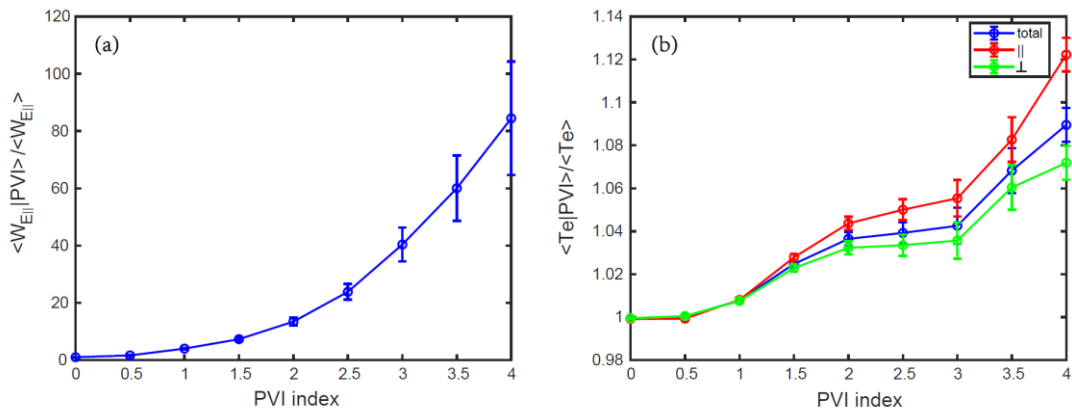
323

324 **Figure 3.** (a) Joint PDFs of E_{\parallel} acceleration rate and the local magnetic field scale L_{dB} ;

325 (b) the average $W_{E_{\parallel}}$ as a function of L_{dB} ; (c) the average L_{dB} as a function of

326 $W_{E_{\parallel}}/(W_{E_{\parallel}})_{rms}$, here $(W_{E_{\parallel}})_{rms}$ is the root mean square of $W_{E_{\parallel}}$; The vertical bars in panels

327 (b) and (c) represent the standard errors of the mean.



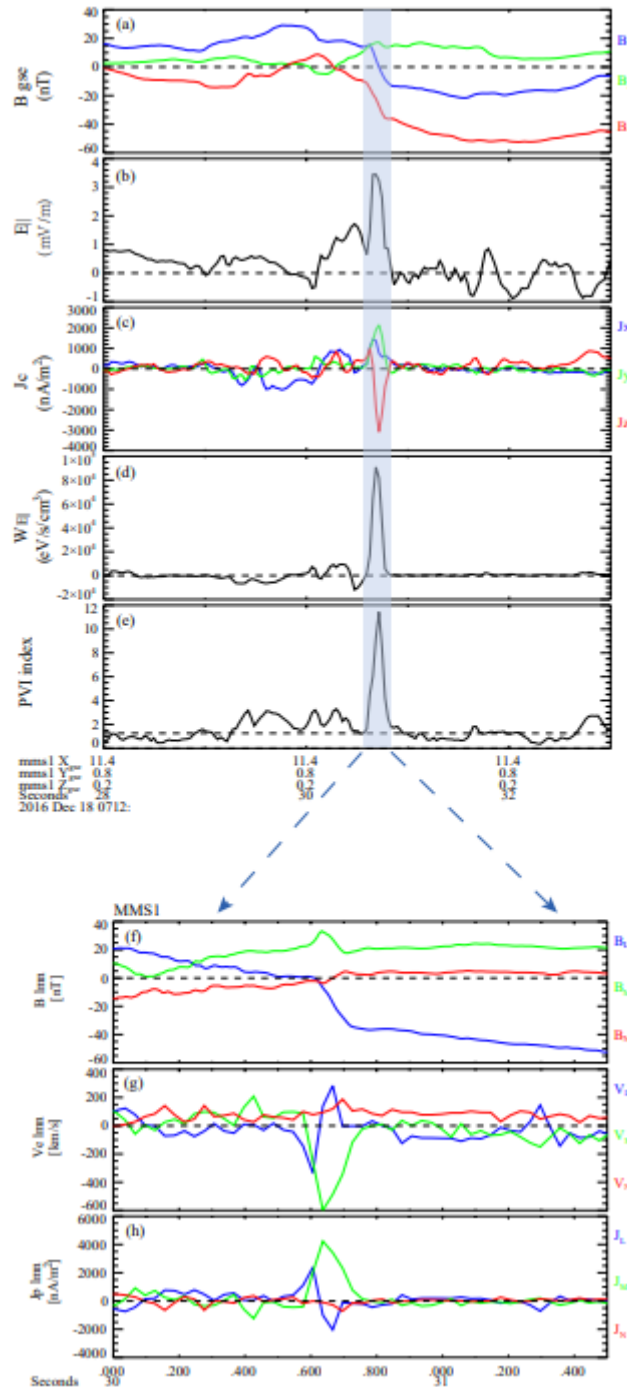
328

329 **Figure 4.** Average E_{\parallel} acceleration rate (a) and electron temperature (b) conditioned on

330 the binned PVI index. The average $W_{E_{\parallel}}$ is normalized by the averaged value in the entire

331 interval. The electron temperature is normalized by $\langle T_e \rangle$ in a moving window with
 332 duration of 4 s, equivalent to approximately 10 d_i . The vertical bars represent the
 333 standard error of the mean.

334



335

336 **Figure 5.** An example of the intense $E_{||}$ accelerate event. From the top to bottom are:
 337 (a) three components of the magnetic field; (b) parallel electric field; (c) electric current
 338 density; (d) $E_{||}$ acceleration rate; (e) PVI Index. The shaded area highlights a significant

339 electron accelerate by E_{\parallel} within a coherent structure. The expanded view displays the
340 (f) magnetic field; (g) electron bulk velocity and (h) current density in the LMN
341 coordinate system around the coherent structure.

342

343 **References**

344 [1] Afshari, A. S., Howes, G. G., Kletzing, C. A., Hartley, D. P., & Boardsen, S. A.
345 (2021). The importance of electron Landau damping for the dissipation of turbulent
346 energy in terrestrial magnetosheath plasma. *Journal of Geophysical Research: Space*
347 *Physics*, 126(12), e2021JA029578. <https://doi.org/10.1029/2021JA029577>

348 [2] Alexandrova, O., & Saur, J. (2008). Alfvén vortices in Saturn's magnetosheath:
349 Cassini observations. *Geophysical Research Letters*, 35(15).
350 <https://doi.org/10.1029/2008GL034411>

351 [3] Bandyopadhyay, R., Matthaeus, W. H., Parashar, T. N., Yang, Y., Chasapis, A., Giles,
352 B. L., Gershman, D. J., Pollock, C. J., Russell, C. T., Strangeway, R. J., Torbert, R. B.,
353 Moore, T. E., & Burch, J. L. (2020). Statistics of kinetic dissipation in Earth's
354 magnetosheath: MMS observations. *Physical Review Letters*, 124(25), 255101.
355 <https://doi.org/10.1103/PhysRevLett.124.255101>

356 [4] Bowen, T. A., Chandran, B. D., Squire, J., Bale, S. D., Duan, D., Klein, K. G., Larson,
357 D., Mallet, A., McManus, M. D., Meyrand, R., et al. (2022). In Situ Signature of
358 Cyclotron Resonant Heating in the Solar Wind. *Physical Review Letters*, 129(16),
359 165101.

360 [5] Büchner, J., & Zelenyi, L. M. (1989). Regular and chaotic charged particle motion
361 in magnetotail-like field reversals: 1. Basic theory of trapped motion. *Journal of*
362 *Geophysical Research Space Physics*, 94(A9), 11821-11842.
363 <https://doi.org/10.1029/JA094iA09p11821>

364 [6] Chandran, B., Li, B., Rogers, B., Quataert, E., & Germaschewski, K. (2010).
365 Perpendicular ion heating by low-frequency Alfvén-wave turbulence in the solar wind.
366 *The Astrophysical Journal*, 720(1). <https://doi.org/10.1088/0004-637X/720/1/503>

367 [7] Chanteur, G. (1998). Spatial interpolation for four spacecraft: Theory. In G.

368 Paschmann, P. W. Daly (Eds.), Analysis methods for multi-spacecraft data (p. 349).
369 Noordwijk, Netherlands: ESA Publ. Div.

370 [8] Chasapis, A., Retinò, A., Sahraoui, F., Vaivads, A., Khotyaintsev, Y. V., Sundkvist,
371 D., Greco, A., Valvo, L. S., & Canu, P. (2015). Thin current sheets and associated
372 electron heating in turbulent space plasma. *The Astrophysical Journal Letters*, 804(1),
373 L1. <https://doi.org/10.1088/2041-8205/804/1/L1>

374 [9] Chen, C. H. K. (2016). Recent progress in astrophysical plasma turbulence from
375 solar wind observations. *Journal of Plasma Physics*, 82(6).
376 <https://doi.org/10.1017/S0022377816001124>

377 [10] Chen, C. H. K., Klein, K. G., & Howes, G. G. (2019). Evidence for electron Landau
378 damping in space plasma turbulence. *Nature communications*, 10(1), 1-8.
379 <https://doi.org/10.1038/s41467-019-08435-3>

380 [11] Dahlin, J. T., Drake, J. F., & Swisdak, M. (2014). The mechanisms of electron
381 heating and acceleration during magnetic reconnection. *Physics of Plasmas*, 21(9),
382 092304. <https://doi.org/10.1063/1.4894484>

383 [12] Dmitruk, P., Matthaeus, W. H., & Lanzerotti, L. J. (2004a). Discrete modes and
384 turbulence in a wave-driven strongly magnetized plasma. *Geophysical Research Letters*,
385 31(21). <https://doi.org/10.1029/2004GL021119>

386 [13] Dmitruk, P., Matthaeus, W. H., & Seenu, N. (2004b). Test particle energization by
387 current sheets and nonuniform fields in magnetohydrodynamic turbulence. *The*
388 *Astrophysical Journal*, 617(1), 667. <https://doi.org/10.1086/425301>

389 [14] Ergun, R. E., Tucker, S., Westfall, J., Goodrich, K. A., Malaspina, D. M., Summers,
390 D., Wallace, J., Karlsson, M., Mack, J., Brennan, N., Pyke, B., Withnell, P., Torbert, R.,
391 Macri, J., Rau, D., Dors, I., Needell, J., Lindqvist, P. -A., Olsson, G., Cully, C. M. (2016).
392 The axial double probe and fields signal processing for the MMS mission. *Space*
393 *Science Reviews*, 199(1), 167–188. <https://doi.org/10.1007/s11214-014-0115-x>

394 [15] Gary, S. P., Winske, D., & Hesse, M. (2000). Electron temperature anisotropy
395 instabilities: Computer simulations. *Journal of Geophysical Research: Space Physics*,
396 105(A5), 10751-10759. <https://doi.org/10.1029/1999JA000322>

397 [16] Greco, A., Matthaeus, W. H., Perri, S., Osman, K. T., Servidio, S., Wan, M., &

398 Dmitruk, P. (2018). Partial variance of increments method in solar wind observations
399 and plasma simulations. *Space Science Reviews*, 214(1), 1-27.
400 <https://doi.org/10.1007/s11214-017-0435-8>

401 [17] Greco, A., Matthaeus, W. H., Servidio, S., Chuychai, P., & Dmitruk, P. (2009).
402 Statistical analysis of discontinuities in solar wind ACE data and comparison with
403 intermittent MHD turbulence. *The Astrophysical Journal*, 691(2), L111.
404 <https://doi.org/10.1088/0004-637X/691/2/L111>

405 [18] He, J., Pei, Z., Wang, L., Tu, C., Marsch, E., Zhang, L., & Salem, C. (2015).
406 Sunward propagating Alfvén waves in association with sunward drifting proton beams
407 in the solar wind. *The Astrophysical Journal*, 805(2), 176. [https://doi.org/10.1088/0004-](https://doi.org/10.1088/0004-637X/805/2/176)
408 [637X/805/2/176](https://doi.org/10.1088/0004-637X/805/2/176)

409 [19] He, J., Wang, L., Tu, C., Marsch, E., & Zong, Q. (2015). Evidence of Landau and
410 cyclotron resonance between protons and kinetic waves in solar wind turbulence. *The*
411 *Astrophysical Journal Letters*, 800(2), L31. [https://doi.org/10.1088/2041-](https://doi.org/10.1088/2041-8205/800/2/L31)
412 [8205/800/2/L31](https://doi.org/10.1088/2041-8205/800/2/L31)

413 [20] Howes, G. G. (2017). A prospectus on kinetic heliophysics. *Physics of Plasmas*,
414 24(5), 055907. <https://doi.org/10.1063/1.4983993>

415 [21] Huang, S. Y., Sahraoui, F., Retinò, A., Le Contel, O., Yuan, Z. G., Chasapis, A.,
416 Aunai, N., Breuillard, H., Deng, X. H., Zhou, M., et al. (2016). MMS observations of
417 ion-scale magnetic island in the magnetosheath turbulent plasma. *Geophysical*
418 *Research Letters*, 43(15), 7850-7858. <https://doi.org/10.1002/2016GL07003>

419 [22] Huang, S. Y., Du, J. W., Sahraoui, F., Yuan, Z. G., He, J. S., Zhao, J. S., Le Contel,
420 O., Breuillard, H., Wang, D. D., Yu, X. D., et al. (2017a). A statistical study of kinetic-
421 size magnetic holes in turbulent magnetosheath: MMS observations. *Journal of*
422 *Geophysical Research: Space Physics*, 122(8), 8577-8588.
423 <https://doi.org/10.1002/2017JA024415>

424 [23] Huang, S. Y., Sahraoui, F., Yuan, Z. G., He, J. S., Zhao, J. S., Le Contel, O., Deng,
425 X. H., Zhou, M., Fu, H. S., Shi, Q.Q., et al. (2017b). Magnetospheric multiscale
426 observations of electron vortex magnetic hole in the turbulent magnetosheath plasma.
427 *The Astrophysical Journal Letters*, 836(2), L27. <https://doi.org/10.3847/2041->

428 [8213/aa5f50](https://doi.org/10.3847/2041-8213/aba263)

429 [24] Huang, S. Y., Zhang, J., Sahraoui, F., Yuan, Z. G., Deng, X. H., Jiang, K., Xu, S.
430 B., Wei, Y. Y., He, L. H., & Zhang, Z. H. (2020). Observations of magnetic field line
431 curvature and its role in the space plasma turbulence. *The Astrophysical Journal Letters*,
432 898(1), L18. <https://doi.org/10.3847/2041-8213/aba263>

433 [25] Huang, S. Y., Zhang, J., Yuan, Z. G., Jiang, K., Wei, Y. Y., Xu, S. B., et al. (2022).
434 Intermittent dissipation at kinetic scales in the turbulent reconnection outflow.
435 *Geophysical Research Letters*, 49, e2021GL096403.
436 <https://doi.org/10.1029/2021GL096403>

437 [26] Isenberg, P. A. (2001). The kinetic shell model of coronal heating and acceleration
438 by ion cyclotron waves: 2. Inward and outward propagating waves. *Journal of*
439 *Geophysical Research: Space Physics*, 106(A12), 29249-29260.
440 <https://doi.org/10.1029/2001JA000176>

441 [27] Isenberg, P. A., & Hollweg, J. V. (1983). On the preferential acceleration and
442 heating of solar wind heavy ions. *Journal of Geophysical Research: Space Physics*,
443 88(A5), 3923-3935. <https://doi.org/10.1029/JA088iA05p03923>

444 [28] Kiyani, K. H., Osman, K. T., & Chapman, S. C. (2015). Dissipation and heating in
445 solar wind turbulence: From the macro to the micro and back again. *Philosophical*
446 *Transactions of the Royal Society A: Mathematical, Physical and Engineering Sciences*,
447 373(2041), 20140155. <https://doi.org/10.1098/rsta.2014.0155>

448 [29] Klein, K. G., Howes, G. G., & TenBarge, J. M. (2017). Diagnosing collisionless
449 energy transfer using field-particle correlations: gyrokinetic turbulence. *Journal of*
450 *Plasma Physics*, 83(4). <https://doi.org/10.1017/S0022377817000563>

451 [30] Kress, B. T., Hudson, M. K., Looper, M. D., Albert, J., Lyon, J. G., & Goodrich,
452 C. C. (2007). Global MHD test particle simulations of > 10 MeV radiation belt electrons
453 during storm sudden commencement. *Journal of Geophysical Research: Space Physics*,
454 112(A9). <https://doi.org/10.1029/2006JA012218>

455 [31] Lindqvist, P. A., Olsson, G., Torbert, R. B., King, B., Granoff, M., Rau, D., Needell,
456 G., Turco, S., Dors, I., Beckman, P., et al. (2016). The spin-plane double probe electric
457 field instrument for MMS. *Space Science Reviews*, 199(1), 137-165.

458 <https://doi.org/10.1007/s11214-014-0116-9>

459 [32] Ma, W., Zhou, M., Zhong, Z., & Deng, X. (2020). Electron acceleration rate at
460 dipolarization fronts. *The Astrophysical Journal*, 903(2), 84.
461 <https://doi.org/10.3847/1538-4357/abb8cc>

462 [33] Ma, W., Zhou, M., Zhong, Z., & Deng, X. (2022). Contrasting the Mechanisms of
463 Reconnection-driven Electron Acceleration with In Situ Observations from MMS in the
464 Terrestrial Magnetotail. *The Astrophysical Journal*, 931(2), 135.
465 <https://doi.org/10.3847/1538-4357/ac6be6>

466 [34] Man, H., Zhou, M., Zhong, Z., & Deng, X. (2022). Intense energy conversion
467 events at the magnetopause boundary layer. *Geophysical Research Letters*, 49(8),
468 e2022GL098069. <https://doi.org/10.1029/2022GL098069>

469 [35] Marsch, E., & Tu, C. Y. (2001). Evidence for pitch angle diffusion of solar wind
470 protons in resonance with cyclotron waves. *Journal of Geophysical Research: Space*
471 *Physics*, 106(A5), 8357-8361. <https://doi.org/10.1029/2000JA000414>

472 [36] Matthaeus, W. H., Wan, M., Servidio, S., Greco, A., Osman, K. T., Oughton, S., &
473 Dmitruk, P. (2015). Intermittency, nonlinear dynamics and dissipation in the solar wind
474 and astrophysical plasmas. *Philosophical Transactions of the Royal Society A:*
475 *Mathematical, Physical and Engineering Sciences*, 373(2041), 20140154.
476 <https://doi.org/10.1098/rsta.2014.0154>

477 [37] Osman, K. T., Matthaeus, W. H., Gosling, J. T., Greco, A., Servidio, S., Hnat, B.,
478 Chapman, S. C., & Phan, T. D. (2014). Magnetic reconnection and intermittent
479 turbulence in the solar wind. *Physical Review Letters*, 112(21), 215002.
480 <https://doi.org/10.1103/PhysRevLett.112.215002>

481 [38] Osman, K. T., Matthaeus, W. H., Wan, M., & Rappazzo, A. F. (2012). Intermittency
482 and local heating in the solar wind. *Physical review letters*, 108(26), 261102.
483 <https://doi.org/10.1103/PhysRevLett.108.261102>

484 [39] Pollock, C., Moore, T., Jacques, A., Burch, J., Gliese, U., Saito, Y., Omoto, T.,
485 Avanov, L., Barrie, A., Coffey, V., et al. (2016). Fast plasma investigation for
486 magnetospheric multiscale. *Space Science Reviews*, 199(1), 331-406.
487 <https://doi.org/10.1007/s11214-016-0245-4>

488 [40] Retinò, A., Sundkvist, D., Vaivads, A., Mozer, F., André, M., & Owen, C. J. (2007).
489 In situ evidence of magnetic reconnection in turbulent plasma. *Nature Physics*, 3(4),
490 235-238. <https://doi.org/10.1038/nphys574>

491 [41] Russell, C. T., Anderson, B. J., Baumjohann, W., Bromund, K. R., Dearborn, D.,
492 Fischer, D., Le, G., Leinweber, H. K., Leneman, D., Magnes, W., et al. (2016). The
493 magnetospheric multiscale magnetometers. *Space Science Reviews*, 199(1), 189-256.
494 <https://doi.org/10.1007/s11214-014-0057-3>

495 [42] Sahraoui, F., Goldstein, M. L., Robert, P., & Khotyaintsev, Y. V. (2009). Evidence
496 of a cascade and dissipation of solar-wind turbulence at the electron gyroscale. *Physical*
497 *Review Letters*, 102(23), 231102. <https://doi.org/10.1103/PhysRevLett.102.231102>

498 [43] Vech, D., Klein, K. G., & Kasper, J. C. (2017). Nature of stochastic ion heating in
499 the solar wind: testing the dependence on plasma beta and turbulence amplitude. *The*
500 *Astrophysical Journal Letters*, 850(1), L11. <https://doi.org/10.3847/2041-8213/aa9887>

501 [44] Wang, Y., Bandyopadhyay, R., Chhiber, R., Matthaeus, W. H., Chasapis, A., Yang,
502 Y., Wilder, F. D., Gershman, D. J., Giles, B. L., Pollock, C. J., et al. (2021). Statistical
503 survey of collisionless dissipation in the terrestrial magnetosheath. *Journal of*
504 *Geophysical Research: Space Physics*, 126(6), e2020JA029000.
505 <https://doi.org/10.1029/2020JA029000>

506 [45] Yao, S. T., Shi, Q. Q., Guo, R. L., Yao, Z. H., Tian, A. M., Degeling, A. W., Sun,
507 W. J., Liu, J., Wang, X. G., Zong, Q. G., et al. (2018). Magnetospheric Multiscale
508 observations of electron scale magnetic peak. *Geophysical Research Letters*, 45(2),
509 527-537. <https://doi.org/10.1002/2017GL075711>

510 [46] Zhong, Z. H., Zhou, M., Huang, S. Y., Tang, R. X., Deng, X. H., Pang, Y., & Chen,
511 H. T. (2019). Observations of a kinetic-scale magnetic hole in a reconnection diffusion
512 region. *Geophysical Research Letters*, 46(12), 6248-6257.
513 <https://doi.org/10.1029/2019GL082637>

514 [47] Zhong, Z. H., Zhou, M., Tang, R. X., Deng, X. H., Turner, D. L., Cohen, I. J., Pang,
515 Y., Man, H. Y., Russell, C. T., Giles, B. L., et al. (2020). Direct evidence for electron
516 acceleration within ion-scale flux rope. *Geophysical Research Letters*, 47(1),
517 e2019GL085141. <https://doi.org/10.1029/2019GL085141>

518 [48] Zhou, M., El-Alaoui, M., Lapenta, G., Berchem, J., Richard, R. L., Schriver, D.,
519 & Walker, R. J. (2018). Suprathermal electron acceleration in a reconnecting
520 magnetotail: Large-scale kinetic simulation. *Journal of Geophysical Research: Space*
521 *Physics*, 123(10), 8087-8108. <https://doi.org/10.1029/2018JA025502>

522 [49] Zhou, M., Man, H. Y., Deng, X. H., Pang, Y., Khotyaintsev, Y., Lapenta, G., Yi, Y.
523 Y., Zhong, Z. H., Ma, W. Q. (2021). Observations of secondary magnetic reconnection
524 in the turbulent reconnection outflow. *Geophysical Research Letters*, 48(4),
525 e2020GL091215. <https://doi.org/10.1029/2020GL091215>

526